University of Padova

Department of Information Engineering
Master Degree in Bioengineering

MASTER THESIS

Comparison of algorithms for 3D arteries segmentations on WBMRA images

Student:
Giulio Degano

Supervisor:
Prof. Alfredo Ruggeri
Co-supervisors:
Prof. Emanuele Trucco
Phd Andrew McNeil

Academic year 2015/2016

To my parents
To Isotta

I progettisti sgobbano
curvi sui tavoli da disegno:
una cifra sbagliata e le cittá del nemico
restano incolumi
Bertolt Brecht

Abstract

Different methods have been proposed in literature to solve the problem of segmentation of vascular structures. Here, we present a comparison of four different solutions: the level set method and three classifiers that use hand crafted features, two based on simple threshold and one on SVM. We first take a look at the theory behind each techniques then we explain how we implemented them in our work in order to create an automatic segmentation method that can be applied inter-patient. The data set is given by Ninewells Hospital in Dundee and this project has been developed during an Erasmus program at the CVIP department of Dundee University.

CONTENTS

1 Introduction **9**
- 1.1 Project Overview . . . 9
  - 1.1.1 Motivation . . . 9
  - 1.1.2 Computer-Assisted Analysis project . . . 9
- 1.2 Image Modality: MRI Angiography . . . 10
- 1.3 Project Aims . . . 13

2 Methods **15**
- 2.1 First step in object detection . . . 15
- 2.2 Level set . . . 17
  - 2.2.1 Chan Vese Model . . . 18
- 2.3 Enhancement Filters . . . 19
  - 2.3.1 Frangi Filter . . . 21
  - 2.3.2 OOF Filter . . . 24

3 Algorithms **27**
- 3.1 Dice coefficient . . . 27
- 3.2 Level set . . . 28
  - 3.2.1 Initilaization of ϕ_0 . . . 30
- 3.3 Enhancement filters . . . 31
  - 3.3.1 Support Vector Machines . . . 32

4 Results **37**
- 4.1 Station 1 . . . 37
  - 4.1.1 Level set . . . 38
  - 4.1.2 Threshold on Frangi and OOF . . . 38
  - 4.1.3 SVM . . . 42
- 4.2 Results . . . 42

4.3 Station 2 . . . 43
4.3.1 Level set . . . 44
4.3.2 Threshold on Frangi and OOF . . . 44
4.3.3 SVM . . . 48
4.4 Results . . . 48
4.5 Station 3 . . . 49
4.5.1 Level set . . . 50
4.5.2 Threshold on Frangi and OOF . . . 50
4.5.3 SVM . . . 54
4.6 Results . . . 54
4.7 Station 4 . . . 55
4.7.1 Level set . . . 56
4.7.2 Threshold on Frangi and OOF . . . 56
4.7.3 SVM . . . 60
4.8 Results . . . 60
4.9 Summary and conclusions . . . 61

5 Future work **63**
5.1 High level filters . . . 64
5.1.1 Filter learning . . . 64
5.2 Conclusions . . . 66

Image links **67**

References **71**

CHAPTER

1

INTRODUCTION

1.1 Project Overview

1.1.1 Motivation

Cardiovascular diseases (CVDs) are the leading cause of death globally, with 42% of all deaths in Europe in 2014 resulting from CVD.. Each year they cause over 4 million death in EU and the approximate cost to the European economy it is about €196 billion due to healthcare, informal care and productivity losses [1]. For this reason there is a strong focus currently on researching ways to improve the methods of diagnosing CVD early, staging it's severity and distribution as is done for cancer, and thereby improving the quality of long-term treatments, and improving patient outcomes.

1.1.2 Computer-Assisted Analysis project

This work is part of a project called *"Computer-Assisted Analysis of Arterial Narrowing in Whole Body MRA"* conduct by the Phd Andrew McNeil under the supervision of Professor Emanuele Trucco from University of Dundee with the aim of develop an automated software solution for grading cardiovascular disease from contrast-enhanced Whole-Body Magnetic Resonance Angiography examination.
The project involves several key parts; first the acquisition of whole body MRA scans of patients exhibiting different degrees of periperal arterial disease (PAD), which was enabled through a collaboration with the Cardiovascular and Diabetes Imaging Research Unit at Ninewells Hospital, Dundee. Secondly, the pre and post-contrast scans were registered for subsequent subtraction using an automated tool provided by the industrial partner Toshiba Medical.
After this first stage the task is to examine vessel enhancement and segmentation to

support the extraction of centerline and the vessel calibres. These last measurements are then compare to ground truth annotations of stenosis severity.
The primary focus of this project was on the automated methods for arterial segmentation from the subtracted whole body datasets. We will begin by explaining the context of this work in the larger project, and the key concepts involved.

1.2 Image Modality: MRI Angiography

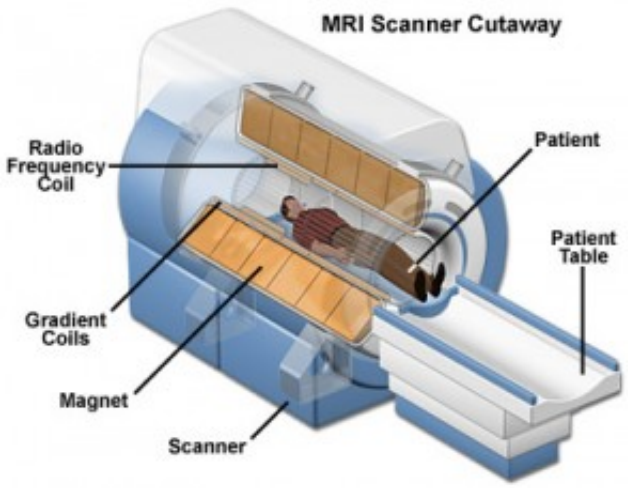

Figure 1.1: Scanner MRI

The image modality that have been used is a contrast-enhanced Whole-Body Magnetic Resonance Angiography, which is a perfect and non-invasive imaging method for the evaluation of CVDs throughout the entire body.
In Fig.1.1 we can see an MRI scanner. The patient is positioned within a strong magnetic filed B_0 generated by the magnet that orients the water molecules in the tissues in the same direction. In this situation of equilibrium, a perturbation B_1 is applied for δ_t seconds and the behavior that bring back the equilibrium is then studied. B_1 has to be:

- small intensity ($\ll B_0$)
- rotating around B_0
- small duration (ms) and in resonance

This impulse generate two different magnetic moments: M_z, longitudinal, with same direction of B_0 and an orthogonal moment M_{xy}. The first one is equal to zero in the instant that B_1 is applied, then grows back at the level of equilibrium; M_{xy} instead is different from zero at the beginning then disappear during the relaxation.
From M_{xy} is possible to evaluate a variation of potential due to the temporal changing of the magnetic flux using Faraday-Lenz law:

$$V_m \propto \frac{\partial \phi}{\partial t}$$

where V_m is the electromotive force measured on the receiver coil and proportional to the variation of flux ϕ.
The presence of a contrast agent in the body in the lumen of the arteries; the channel in which the blood flows modifies the relaxation time of the magnetic moment, this allow different results in pre and post contrast imaging. The subtraction of these volumes is the base concept of angiography.

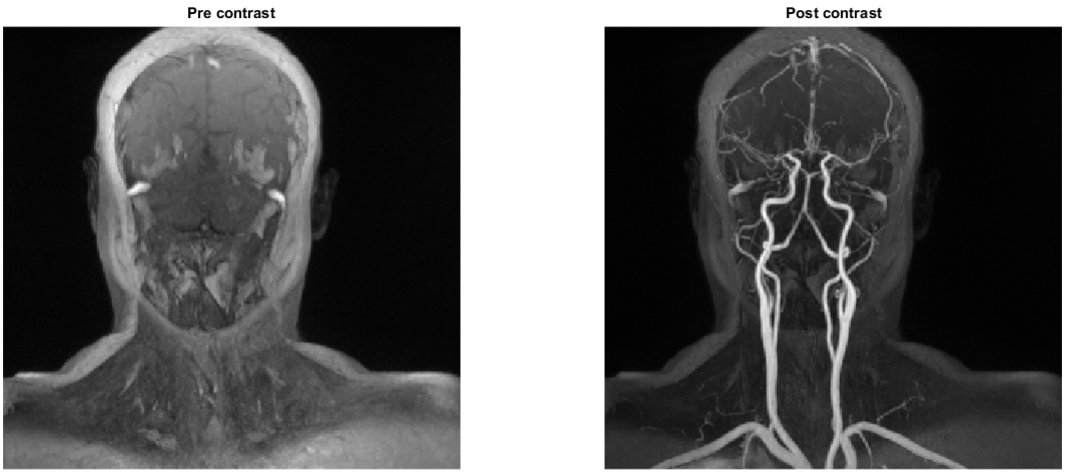

Figure 1.2: Pre and post contrast imaging

In Fig.1.2 we can see the head volumes before and after the injection of the contrast agent. The difference of intensities in the vessels is clearly visible.
The critical procedure is to scan the area of interest at the correct time, that is when the CA has reached his peak; mistiming the scan can results in reduced arterial contrast, or unwanted artifacts such the enhancement of veins.
The whole-body dataset is acquired as a series of four separate scans (head, abdomen, legs, and feet). These volumes can be overlapped to visualize the entire body, although in our study we will work on each station separately. Fig.1.3 shows the procedure of acquisition in which the patient is laying on a movable table while the MRI is acquiring the images. Due to the position of the person inside the instrument we have to define three different reference plane: the sagittal one passing through midline structures such as the navel and spine, the coronal one: a vertical plane that divides the body into ventral and dorsal (belly and back) sections and the transverse one that divides the body into superior and inferior parts. Each plane has to be orthogonal to the other two. In Fig.1.4 we can see this reference system.

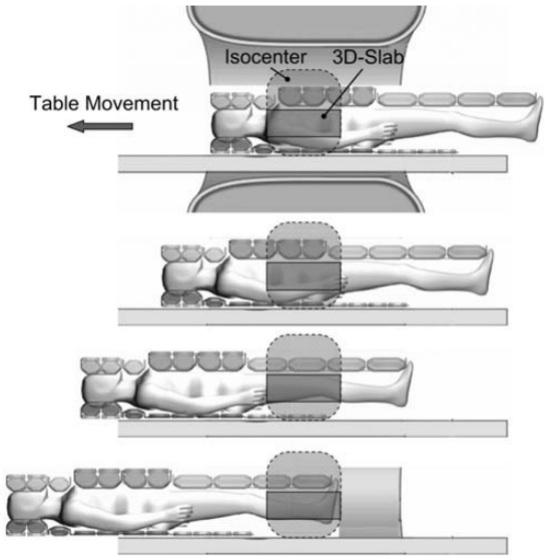

Figure 1.3: WMBRA acquisition, showing image volumes acquired at different stations.

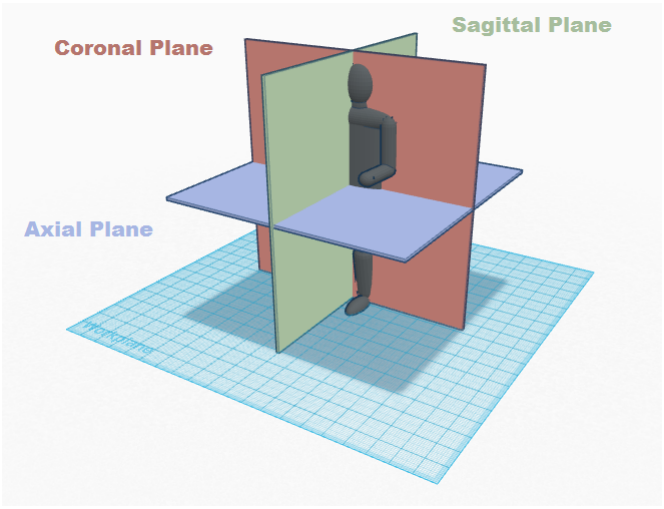

Figure 1.4: Coronal, sagittal and transverse planes on human body.

1.3 Project Aims

One of the primary interests in WBMRA for assessing CVD is its possible application for screening asymptomatic populations, thanks to the fact that the magnetic resonance is safer, without any ionizing radiation (as it is for CTs), and the timing of scans it is around an hour so it is not a invasive instrument.
On the other hand the datasets are typically very large, so subsequent assessment and diagnosis is a time consumiing and costly procedure. For this reason the aim of develop an automated tool for patient selection and for guiding the clinicians on the most problematic areas is a very useful but also challenging task.
As we said before this work is focusing on the segmentation methods for the extraction of arteries from the different stations that we get from MRA. The segmentation of vascular structures is in general very useful for different kind of medical application from diagnosis assistance to surgery planning. This is why it is a fundamental step to the correct visualization of vessels and the quantification of pathologies, as, in our case, stenosis. Careful manual segmentation can often take hours or days to produce a good segmentation of the vascular map, but, by reducing the number of human interaction with the software, it is possible to reduce heavily the time cost of the processing. In the next chapters we will see the method that we decided to follow and the results on our data set.

CHAPTER

2

METHODS

Vascular segmentation is a very specific and challenging problem [2]. First of all vessels structures are very sensitive to the acquisition procedure, the MRA imaging especially is sometimes a very noisy procedure and it can show different kind of artifact (as the one we will discuss in Chapter 3). The size, the curvature and the geometry can vary deeply for different reasons: stents, calcification, stenosis and obviously the position inside our body.
The modern modality of imaging, such as WBMRA ones, have high quality of resolution, they can capture complex vascular structures, but, in the meantime, they collect large volumes of data. To address a well segmentation technique we had to compare the major innovation in sate-of-art literature.

2.1 First step in object detection

In computer vision, the task of edges and object detection as always been challenging, in the last 30 years a lot of different methods have been developed and thanks to the evolution of the computational power of the computer, what in the past was too heavy to process now can easily calculated on a laptop. For this reason, before explaining which techniques are getting more attention in research, we need to take a quick look at the beginning.
A gray image in two, three or M dimension can be seen as a function $f(x_1, x_2, \ldots, x_n) : \Re^n \rightarrow \Re$ that projects each coordinate in a grey value. This function can represent each scanned object with different level of grey intensity in a normalized range between zero and one. In our case the background is darker with an intensity that tends to zero, while the vessels have a gray level near one so they appear brighter.
By exploiting this characteristics the first and more simple edges detector that have been used for segmentation were based on the idea that an object can be extracted

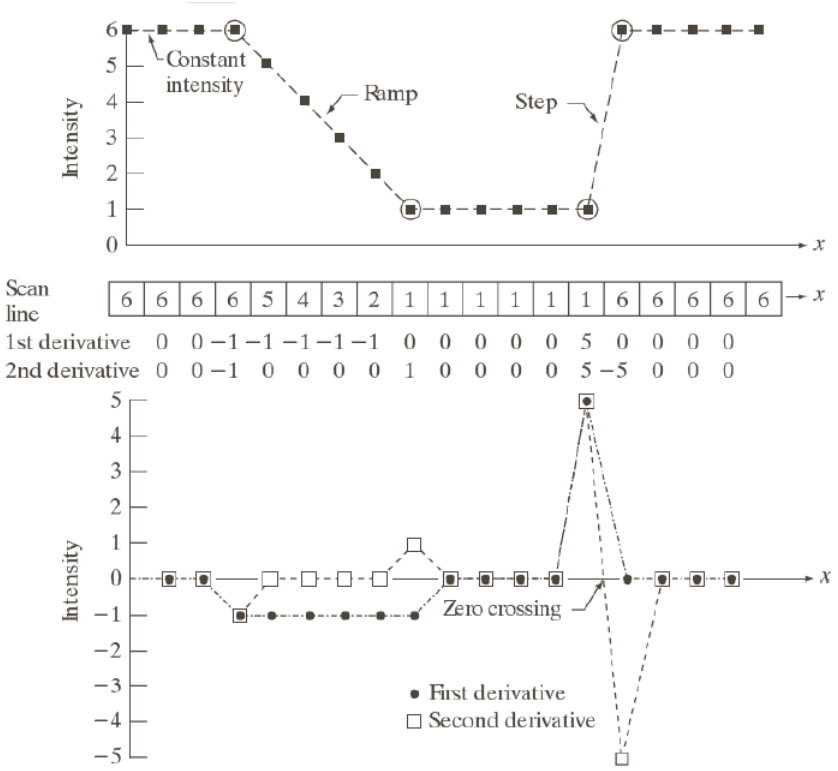

Figure 2.1: Derivative of gray level [3]

from the background thanks to the difference in the intensity. In Fig.2.1 we can see the values on the first and second derivatives in 1D (easier to represent). Thanks to the behavior of these two functions it clearly easy to identify the position of a discontinuity in the image: the peaks and the region different from zero can lead to the definition of the boundaries of an object.
In our case we can define in 3D space the gradient of our volume like

$$\nabla f(x,y,z) = \begin{pmatrix} \frac{\partial f}{\partial x} \\ \\ \frac{\partial f}{\partial y} \\ \\ \frac{\partial f}{\partial z} \end{pmatrix} \approx \begin{bmatrix} f(x,y,z) - f(x-1,y,z) \\ f(x,y,z) - f(x,y-1,z) \\ f(x,y,z) - f(x,y,z-1) \end{bmatrix} = \begin{bmatrix} G_x \\ G_y \\ G_z \end{bmatrix} \tag{2.1}$$

By these equations it is possible to build simple spatial derivative operator that can already detect an object or a structure in a image or volume. The negative aspect of these operators is that they are very sensitive to noise and artifacts. For example a non-vessel structure, that the MRA does not eliminate during the subtraction procedure, will be detected because it exhibits a a strong discontinuity with background. For this reason there was the need to build more specific algorithms for the segmentation of desired structures, so starting by the evaluation of the gradient of an image, different methods have been proposed from the early 90s to the last years.
The study that we conduct is based on the comparison of two principal solutions for segmentation: the first one, called *level set*, has been for years the state of art solution

for a lot of different computer vision task, thanks to the fact that is based on robust and sophisticated mathematical models. After the correct setup of the parameters, this method gives a mask that coincides with the structure that need to be extracted, in our case arteries. The second one is built on more recent filters for the enhancement of vessels, which are called *Frangi* and *Optimally Oriented Flux*. On the contrary of the level set these filters gives a bag of information that can be used in a second step for the final segmentation process. In Chapter 3 we will discuss what kind of algorithms we build to do so.

2.2 Level set

The segmentation using active contour was first proposed in [6] then an extensive research has been done using this methods. The idea of active contour is to evolve an initial curve on the boundaries of an object by controlling external and internal forces. This family of image segmentation methods are typically based on minimizing a cost function which defines when the curve is close to the target and satisfies the boundary conditions.
The level set model tries to solve the optimization problem by embedding the active contour as a constant set (*zero level*) in a function ϕ that evolves in time with speed S. By Lipschitz function we can define the curve C_t as:

$$C_t = \{(x_1, x_2, \ldots, x_n) | \phi(t, x_1, x_2, \ldots, x_n) = 0\} \tag{2.2}$$

so it's behavior in time can be described by a partial differential equation as [7]:

$$\frac{\delta\phi}{\delta t} = |\nabla\phi|\, S, \qquad \phi(0, x_1, x_2, \ldots, x_n) = \phi_0(x_1, x_2, \ldots, x_n)$$

$$\phi(t, x_1, x_2, \ldots, x_n) = d(C_t, x_1, x_2, \ldots, x_n) \tag{2.3}$$

where d represents the signed Euclidean distance from the point $(x_1, x_2, \ldots, x_n)$ to the curve.

Forward Euler For the solution of Equation 2.3 it is necessary to discretize the function $\phi(t, \mathbf{x})$. So there is the need to find a sequence $u_1, u_2, \ldots, u_{Nh}$ where the element u_k of the sequence approximates the solution $\phi(t, \mathbf{x})$ of the differential equation for $t = kh$.
There are different methods to solve this Cauchy problem, here we can see the simplest one called forward Euler. This method uses the Taylor expansion truncated at the first term and obtains the solution:

$$\frac{u_{n+1} - u_n}{\Delta t} = u\phi_u + v\phi_v + w\phi_w \tag{2.4}$$

where $u_0 = \phi(0)$ so we can link the sequence with step Δt. Notice that one critical parameter is always the step Δt, because it can control the expansion of the curve in the level set application.
In Fig.2.2 we can see a graphical idea of the method. Several ways to approach the problem can change the objective function that the algorithm is trying to minimize,

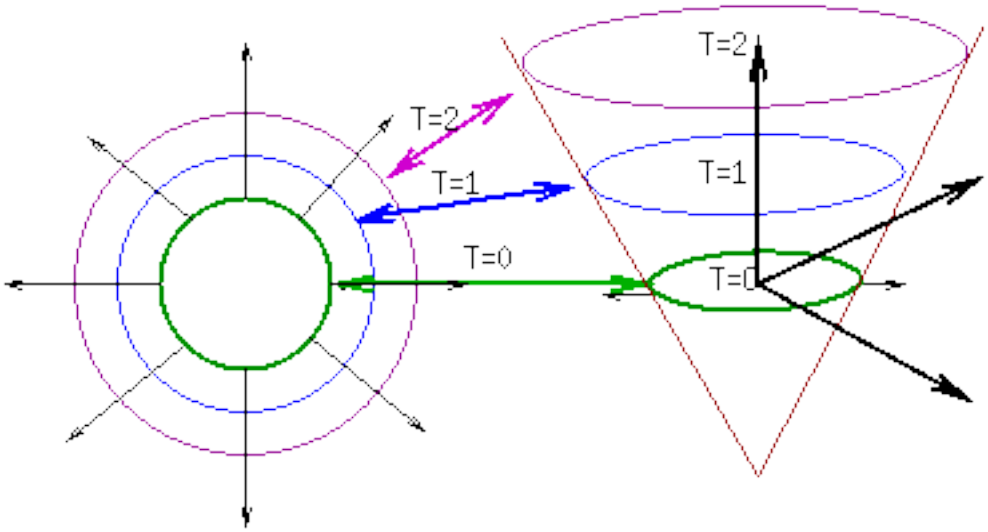

Figure 2.2: Level set method

so, even if the goal is the same, the results can be very different. In this chapter we will analyze the method that is usually used for the extraction and segmentation of object whose edges are not well defined by the gradient. The method is called Chan-Vese model [4] and it's very well implemented for 3D segmentation in [5].

2.2.1 Chan Vese Model

In general, active contour are based on the value of the image gradient, so they can easily detect the edges of an object, generating well-defined boundaries on which to evaluate the internal and external energy. The issue is that this kind of approach does not perform very well in the case of structures with 'smoothed' edges, that is actually what happens for vessel images, where the gradient does not provide a reliable measure for these thin framework.
We define $\Omega \in \Re^n$ as bounded domain (in our case $n = 3$) and a function $I : \Omega \to \Re$ as the bounded image function. Hypothetically Ω can be divided in a set of connected domains by the subtraction $\Omega - C = \cup_{i \in I} \Omega_i$, now it is possible to define two different regions $R_1 = \cup_{i \in I_1} \Omega_i$ and $R_2 = \cup_{i \in I_2} \Omega_i$ that represent respectively the object support and the background support. The functional of the model is:

$$E(\phi, \mu_1, \mu_2) = \lambda_1 \int_\Omega (I - \mu_1)^2 H(\phi) d\Omega + \lambda_2 \int_\Omega (I - \mu_2)^2 (1 - H(\phi)) d\Omega \tag{2.5}$$

$$+ \alpha \int_\Omega H(\phi) d\Omega + \beta \int_\Omega |\nabla H(\phi)| \, d\Omega, \tag{2.6}$$

where μ_1 and μ_2 represent the mean value of the image I respectively in the object support region and background support region. $H(\phi)$ is the Heaviside function.
As we said at the beginning, this model performs very well on some images with fuzzy boundaries, but in the case of complex background the global values of μ_1 and μ_2 can

create problems during the segmentation. Moreover the fact that the algorithm does not evaluate the boundaries term, can make it more inaccurate than one that does, where the tubular structure is well defined.

(a) Initialization in red

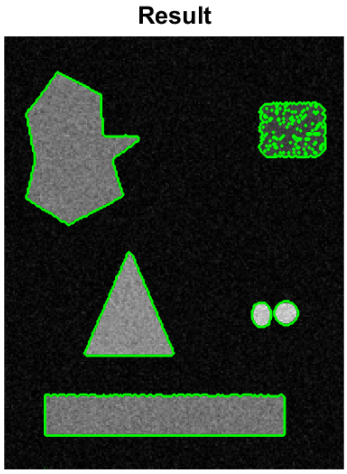

(b) Result contour C in green

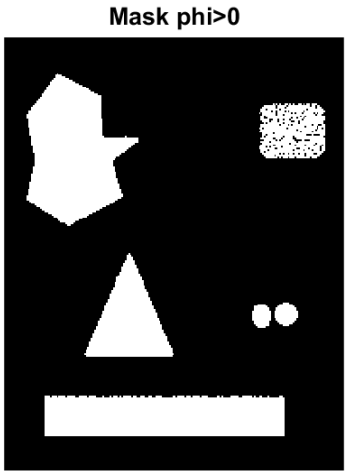

(c) Segmentation

Figure 2.3: Example on synthetic image with noise

It has been shown in literature that this kind of approach has been very useful to evaluate incomplete branches, finalize discontinuities and avoid false detections. The selection of the stopping criterion is always critical, that is why the segmentation of tiny vessels it's always very difficult. Despite that some good results have been achieved especially in 2D DSA images.
In Fig.2.4 we can see the results of the coronarography segmentation in [8].

2.3 Enhancement Filters

The other approach used in this work is the extraction of *features* from MRI volumes by using detectors and filters to evaluate the vessel map on the data. In the literature

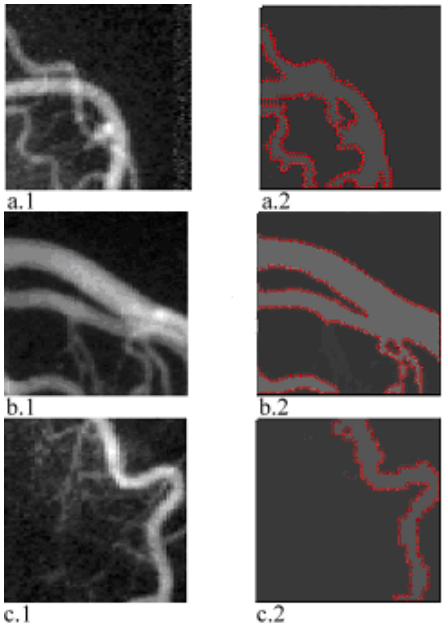

Figure 2.4: Image from Brieva et all. The a.1, b.1 and c.1 are from the original image and a.2 b.2 and c.2 display the level set method

a number of paths have been explored for feature extraction, including: *Local isotropic feature*, *3D local geometry feature* and *2D cross sectional feature* as explained in [2]. These first ones are usually isotropic as they don't use any assumption on directionality, so they can be useful to obtain position and scale of vessels. One first example is based on the hypothesis that vessels are brighter than the background so it's possible to build a robust *intensity maxima* method as in [9].
The 2D cross sectional features, instead, want to give a measure of the compactness of the vessels using only two dimensions. So there is the advantage of down-scaling from the 3D volumes, but this solution can be sensitive to noise and local perturbation.
In this work we decided to proceed with the second way, by proposing derivative features that have been widely used elsewhere in the literature and have been a popular method for detecting vascular patterns due to exploiting local geometry information. One of the most famous is the hessian-based filter used for discriminating between blob-like, plate-like and tubular-like structures in [10]. These filters utilize Gaussian derivatives with different SD so it is possible to evaluate the response of vessels with different size and positions. The main problem is that the responses are poor near bifurcations so there is more difficulties to use those features for automatic segmentation. Despite this fact this method has been a standard approach during the last ten years. In 2009 Law M.W.K. has proposed a more robust filter that use the gradient flux that flows through spheres centered in local voxels to obtain a response in presence of vessels [11].
In the next section we will explain more about these filters, how they work, and what their advantages are.

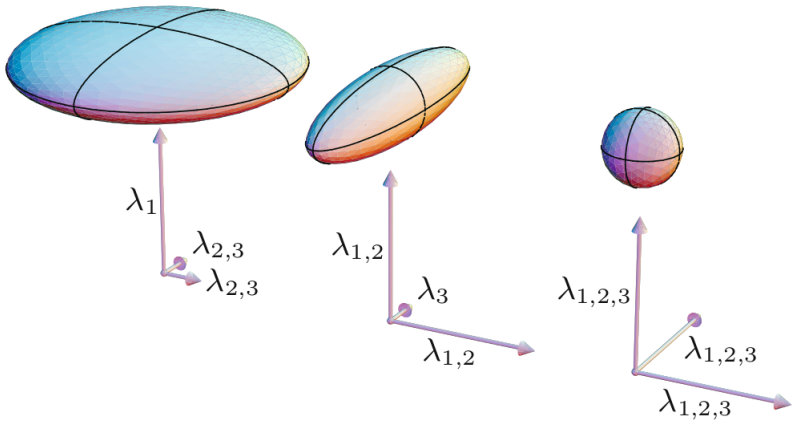

Figure 2.5: Isosurfaces that represent the plate-like line-like and blob-like structures

2.3.1 Frangi Filter

The basic idea of this method is to calculate the local curvature analysing the Hessian function, with the purpose of extracting the main directions in which the structure can be decomposed.
To evaluate the local behavior of the image $I : \Re^n \to \Re$ the second order Taylor expansion is considered around a generic point $\mathbf{x_o}$:

$$I(\mathbf{x_o} + \mathbf{v}, s) \approx I(\mathbf{x_o}, s) + \nabla I(\mathbf{x_o}, s) \cdot \mathbf{v} + \mathbf{v}^T \mathbf{H_s} \mathbf{v} \tag{2.7}$$

where $\nabla I(\mathbf{x_o}, s)$ and $\mathbf{H_s}$ represent respectively the gradient and the Hessian of the image I around $\mathbf{x_o}$ with scale s. Notice that the differential operator is generally *well-posed*, this means that the image is convolved with the first and second derivative of a Gaussian kernel. This function, in fact, can be used to distinguish and measure the contrast between two different regions on scale s.
In this work we proceed with the analysis of the Hessian in three different directions, extracting the eigenvalues λ_i with $i = 1, 2, 3$from the matrix:

$$\mathbf{H_{s,o}} \mathbf{u_{s,i}} = \lambda_{i,s} \mathbf{u_{s,i}} \tag{2.8}$$

where $\mathbf{u_{s,i}}$ represent the relative eigenvector in $\mathbf{x_o}$ on scale s. For the evaluation of the vesselness funtion, we proceed under the hypothesis that a 3D tubular structure has:

$$\begin{gathered} |\lambda_1| \approx 0 \\ |\lambda_1| \ll |\lambda_2| \\ |\lambda_2| \approx |\lambda_3| \end{gathered} \tag{2.9}$$

As we can see in Fig. 2.5 some different cases of ideal structure, as *blob-like*, *plate-like* and *line-like*, have different ratios between eigenvalues. Starting from this distinction we want to evaluate two dissimilarity measures that allow us to characterize the structures. The first one:

$$R_A = \frac{(Largest\ cross\ sectional\ area)/\pi}{Largest\ axis\ semi\text{-}length^2} = \frac{|\lambda_2|}{|\lambda_3|} \tag{2.10}$$

the second one:

$$R_B = \frac{(Volume)/(4\pi/3)}{(Largest\ cross\ sectional\ area/\pi)^{3/2}} = \frac{|\lambda_1|}{\sqrt{|\lambda_3\lambda_2|}} \tag{2.11}$$

Where $R_A \wedge R_B \in [0,1] \subset \Re$ are respectively the deviation from blob-like and plate-like structures.
In the case where the eigenvalues have low modules, another term is introduced, named *second order structurness*, that allows to distinguish the background noise. S is defined as:

$$S = \|\mathbf{H_o}\|_F = \sqrt{trace(\mathbf{H_o}^T\mathbf{H_o})} = \sqrt{\lambda_1^2 + \lambda_2^2 + \lambda_3^2} \tag{2.12}$$

where $\|\mathbf{H_o}\|_F$ is the Frobenius's norm.
Combining 2.10 , 2.11 e 2.12 we obtain the vesselness function:

$$V_o(s) = \begin{cases} 0 & \text{se } \lambda_2 > 0 \vee \lambda_3 > 0 \\ \left(1 - e^{\left(-\frac{R_A^2}{2\alpha^2}\right)}\right) e^{\left(-\frac{R_B^2}{2\beta^2}\right)} \left(1 - e^{\left(-\frac{S^2}{2c^2}\right)}\right) & \text{otherwise} \end{cases} \tag{2.13}$$

where α,β and c are the threshold parameters that controls the three different dissimilarity terms. The equation must be computed on different scale levels so that we can obtain the maximum response between each value of s.
The image I will be elaborate for each point $\mathbf{x_o} \in I$;

$$V_0 = \max_{s_{min} \leq s \leq s_{max}} V_0(s) \tag{2.14}$$

with s_{min} and s_{max} defined in input.
The study by Frangi showed some results on three-dimensional aortiliac MRA dataset comparing the output from a threshold applied on raw volumes and filtered ones.
The Fig. 2.6 shows the MIP of the enhanced images at different scales; we can see that by incrementing the value of s, the smaller vessels disappear with a consistent blurring of the rest of the data. In Fig. 2.7 we can see the renderings obtained using a threshold: the original image, as expected, shows more background artifacts.

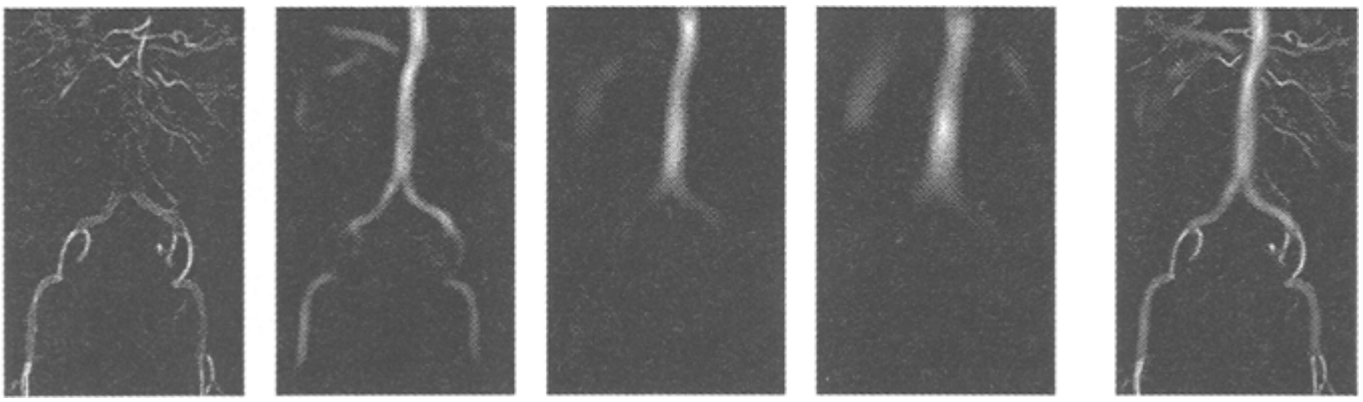

Figure 2.6: We can see from left to right the vesselness at increasing scales. The last one is the results after the selection procedure

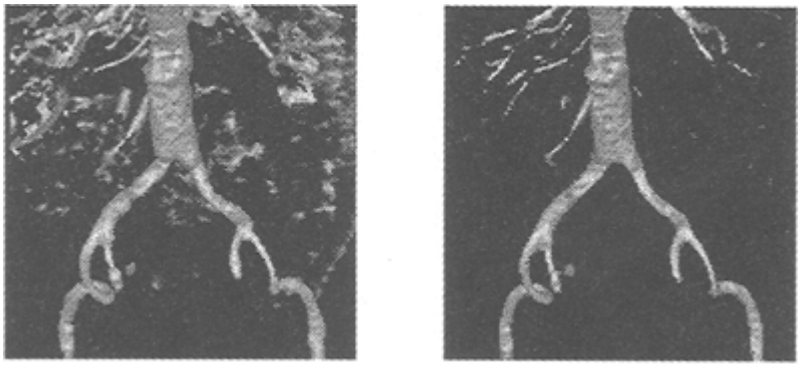

Figure 2.7: Results of thresholding

We have used the same approach on our WBMRA images and we find out, as can be found in literature, that one of the main problem of the Hessian based method is that, in some cases, it merges close vessels and discards smaller vessels as noise. For example, in the following figure you can see the result on the head; it is easy to notice this effect especially if you compare it with Fig. 2.10

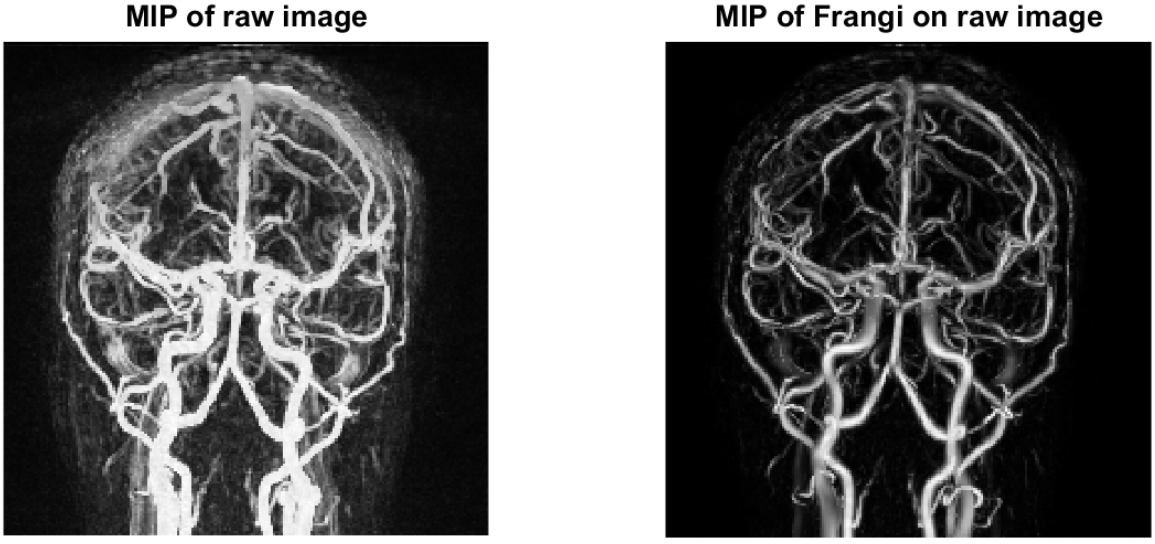

(a) Raw image (b) Enhanced image

Figure 2.8: Example on MRI angiography

2.3.2 OOF Filter

The problem with the second order derivatives of a Gaussian kernel is that these functions have low performances when the edges of an object are not homogenous. In particular this phenomenon happens when two or more structures are nearby the object, due to the effect of the filtering itself. The *optimally oriented flux* is a powerful instrument created by [11] that evaluates a scalar measure of the quantity of flux that flows through a spherical surface. Before computing this value, directional information is extracted by projecting the gradient along "optimal" axes, then the flux measure evaluated. In order to do that the OOF method finds the axes that minimize the oriented flux by evaluating it voxel by voxel on the entire volume. For each of these voxels a sphere with variable radius is built and centered on the voxel, when the sphere touches the edges of the object it produces a response called OOF response. If the voxel is inside the curvilinear structure the response will be positive, otherwise it will be negative.
The outwardly oriented flux along the direction $\hat{\rho}$ has to be computed by firstly projecting the gradient of the image $\mathbf{v}$ along $\hat{\rho}$, then the flux has to be evaluated through the spherical region $\mathrm{S_r}$ with radius r using the definition:

$$f(\mathbf{x}; \mathbf{r}, \hat{\rho}) = \int_{\delta S_r} ((\mathbf{v}(\mathbf{x} + \mathbf{h}) \cdot \hat{\rho})\hat{\rho}) \cdot \hat{n} dA \tag{2.15}$$

where dA is the infinitesimal area of δS_r, $\hat{n}$ is the unit normal to the surface at the position $\mathbf{h} = r\hat{n}$.
As it was for Frangi, also in this case the goal is to obtain the principal eigenvalues for each voxel. Inside the vessel, when the local spherical region with surface δS_r touches the boundaries of the object, $\mathbf{v}$ is aligned in the opposite direction of the unit normal $\hat{n}$ so the eigenvalues $\lambda_1 \leq \lambda_2 \ll 0$. The gradient of the image will be perpendicular to the direction of the curvilinear structure, with a value of $\lambda_3 \approx 0$. In the case where the voxel is in the background, $\mathbf{v}$ will have the same direction of the unit normal to the surface, so the eigenvalue will be $\lambda_3 \gg 0$.
To obtain the maximum response to the OOF while changing the radius r, we proceed with the evaluation of the geometric mean of the eigenvalues as it follows:

$$\boldsymbol{M}(\mathbf{x}; s) = \begin{cases} \sqrt{|\lambda_1(\mathbf{x}, s)\lambda_2(\mathbf{x}, s)|} & \lambda_1(\mathbf{x}, s) \leq \lambda_2(\mathbf{x}, s) < 0 \\ 0 & \text{otherwise} \end{cases} \tag{2.16}$$

where s, as it was for Frangi, represents defined scale factor.
In [11] some synthetic experiments have been conducted and the results showed that OOF was more robust than Hessian based methods in discovering smaller structures and discriminating small separations between vessels. In the next figure we can see the results of this study.

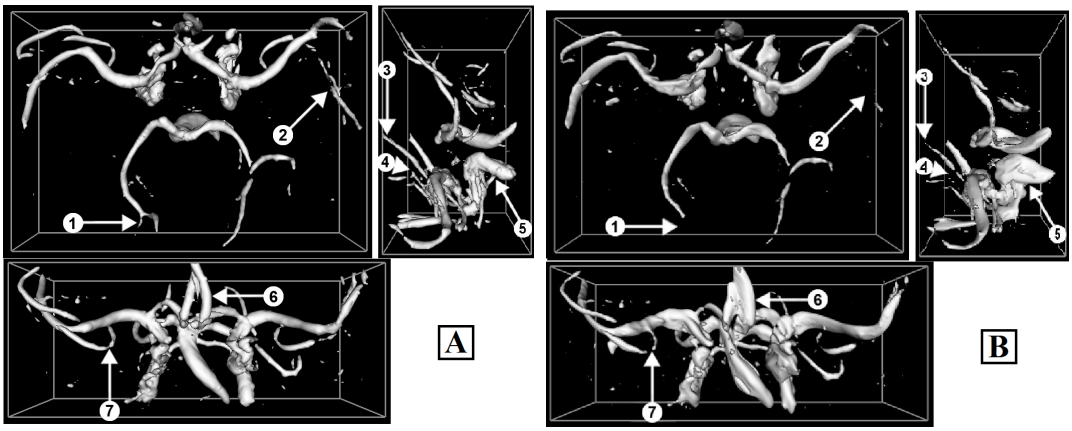

(a) OOF method (b) Hessian method

Figure 2.9: In this figure, as showed from point 1 to 6, we can see the differences between these methods because of the effect that we discussed before.

As we did previously we tested this method and, as expected, we obtained the same conclusions.

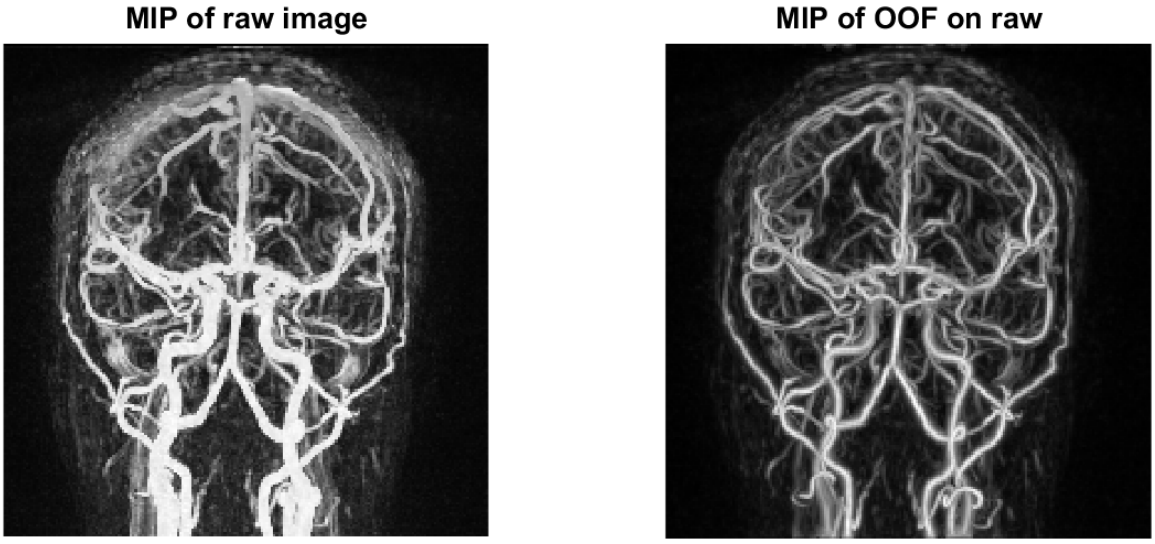

(a) Raw image (b) Enhanced image

Figure 2.10: Example on MRI angiography

CHAPTER

3

ALGORITHMS

Once we had all these methods ready for the implementation we had to decide how to use them for a correct comparison and most of all how to create the right algorithms to express each solution at its best. The approach that we decided to take was to use one patient (called 70020) to select a set of parameters or to find a model for each of the four stations and then test it on a new patient (called 63162).
For the annotations instead there was the need to find a manual method to extract the ground truth. A colleague from the Univeristy of Dundee, Seonaid Robertson, applied a semi automated method for manually segmenting the whole arterial tree of two patients. The methods described in Chapter 2 require additional pre-processing and optimisation in order to be widely applicable to any unseen patient dataset. In the following sections we will discuss the processing steps of each algorithm in more detail, but first we will explain the metric used to carry out the quantitative comparison of each technique.

3.1 Dice coefficient

In the literature one of the most widely used coefficients for evaluating the quality of segmentation is the Sorensen Dice score. This statistic is used to compare the similarity between two segmented areas or volumes, and is given by:

$$DICE = \frac{2\,|X \bigcap Y|}{|X| + |Y|} \tag{3.1}$$

where $|X|$ is the number of all the vessel voxels in the segmentation obtained by automated method, $|Y|$ is the number of all the vessel voxels in the ground truth. The numerator represent the intersection between the two.

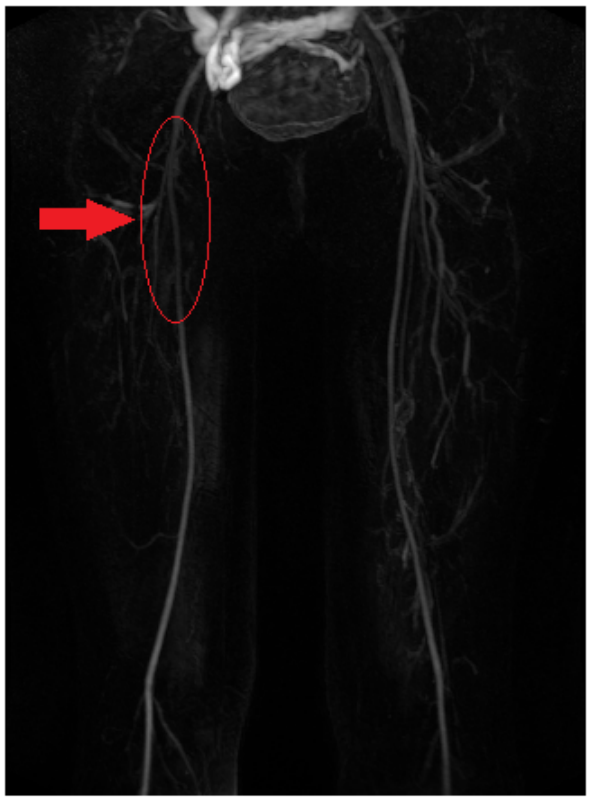

Figure 3.1: Artifact on the legs

Notice that the value $|X \bigcap Y|$ is equal to the number of true positive (TP) that the algorithm has found, so the DICE score can be interpreted as the sum of the percentage of TP in the segmentation and the percentage of TP in all the true vessel voxel.

3.2 Level set

One artifact which is prevalent in our raw data is the variation of signal intensity along the length of some vessels. These may be caused by poor timing of the contrast agent during acquisition, or by various inhomogeneities such as surface coil artefacts (often seen in the legs, as shown in Fig 3.1). To compensate for this we first applied a preprocessing step to each station, in the form of local normalization.
We decided to divide each slice, taken axially, by the Grey level that should be the intensity of the vessel. In order to do so, we took a neighborhood of three slices forward and three backward (for a total sub-volume of seven slices) and evaluated the histogram of the volume, like in Fig. 3.2. Then we hypothesized that the histogram presents a small peak in frequency at higher Grey levels, so we selected an interval between the 70% of the maximum intensity and the maximum itself. In this "reduced" histogram we choose the value with higher frequency x_{best_i} that should be equal to the expected *local vessel intensity*.

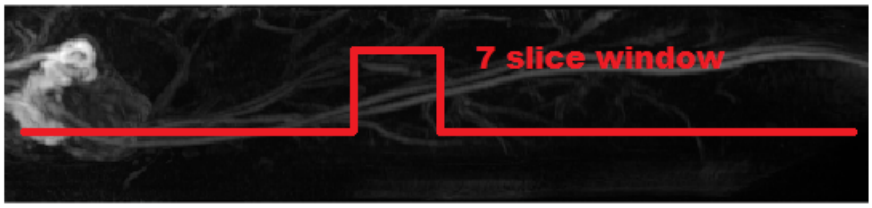

(a) Window

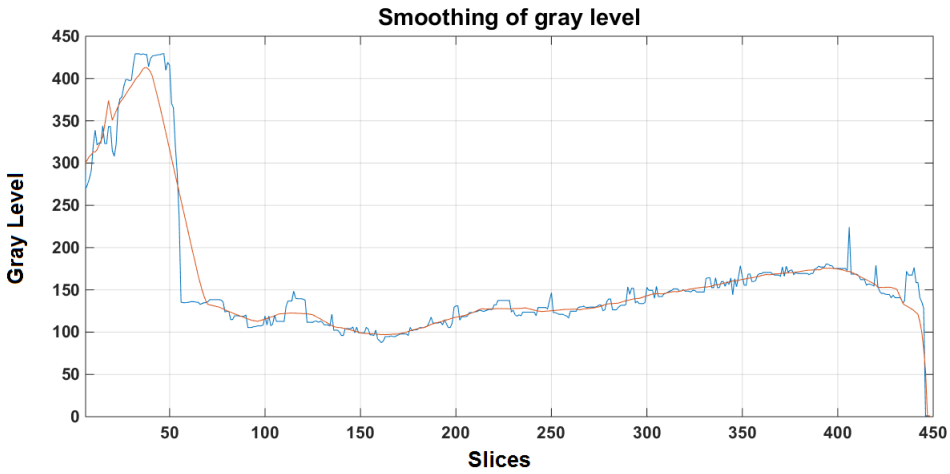

(b) Smoothing

Figure 3.2: Local intensity normalisation procedure

After the computation of x_{best_i} for each slice, the result is a vector $X = [x_{best_1}, \ldots, x_{best_N}]$ with an high grade of irregularity, for this reason we must smooth X in order to avoid discontinuity in the normalized volume. We used the new smoothed value $\hat{x}_{best}$ to divide the original value of the slice as you can see in Fig. 3.2.
An outline of the algorithm used is given in Algorithm 1.:

Data: Volume from the patient
Result: Grey level for each slice
Select axial direction;
for *each slice* **do**
    Take neighbors;
    Select 70% of maximum;
    Evaluate histogram and take highest frequency;
end
Obtain a vector of size = number of slice in axial direction;
Smoothing of the vector;

After this step we used the Toolbox from [5] for the level set segmentation. We created a 3D grid for searching the optimal setting of parameters. In our case we set β, Δt and λ.

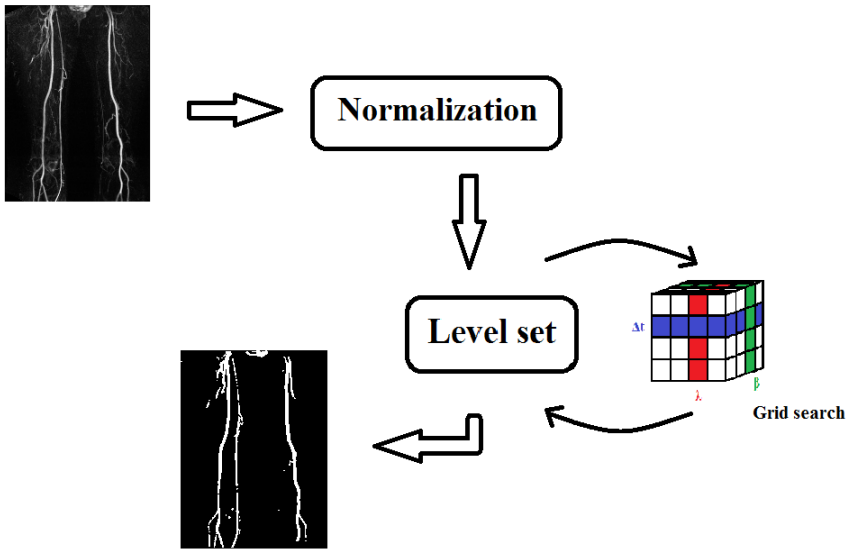

Figure 3.3: Scheme for level set segmentation

3.2.1 Initilaization of ϕ_0

At this point we had a last problem with the initialization of ϕ_0. This choice was critical because it can change the time and the speed of the evolution of the curve so we wanted to find a good compromise that could have been used for all the four stations. So again under the hypothesis that the voxels with higher intensities are belonging to the vessels, we took a set of seed points with high grey levels as ϕ_0.
To keep the process completely automatic, one way to select a threshold for the seed point is to use a multithresh Otsu's method [12]. The goal of this method is to find a value of $N-1$ thresholds that maximize the inter-class variance σ_b when a number N of different classes have been chosen. Here the algorithm with our choice of 11 classes:
Where ω_i and μ_i are respectively probability and variance of class i with the selection

Data: Gray levels of volume I and N
Result: 10 thresholds $t_1, \ldots, t_{10}$
Evaluate histogram and probabilities of each gray level in the volume;
Initialize ω_0 and μ_0 for each class;
for *each possible thresh* **do**
  Compute new ω_i and μ_i ;
  Compute σ_b ;
end
Take max value of σ_b and use selected thresh;

Algorithm 1: Otsu's method

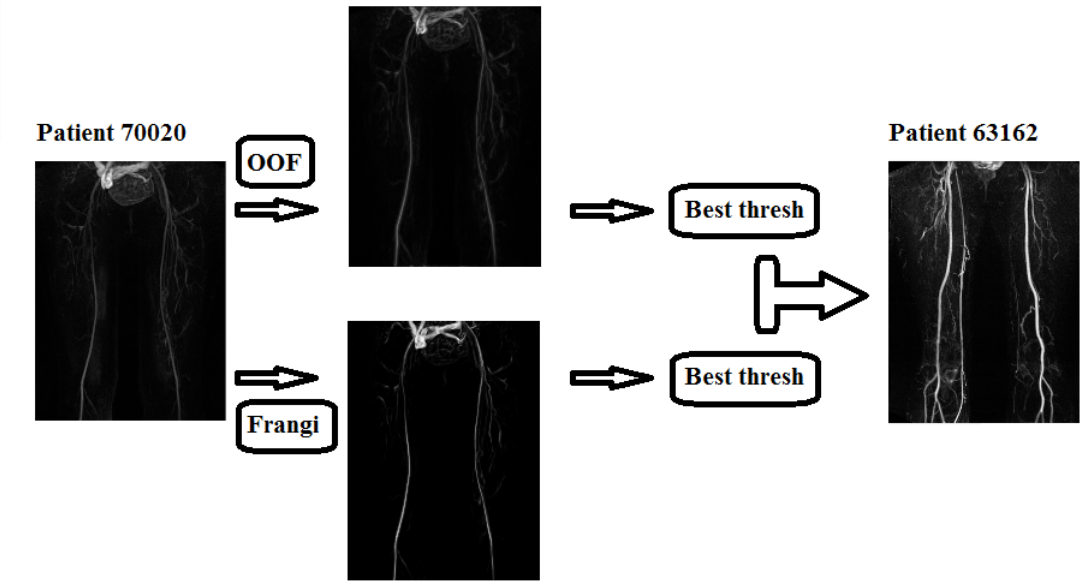

Figure 3.4: Scheme for threshold selection

of $t_1, \ldots, t_{10}$.
After obtaining these values we chose all the voxels with intensity higher than the 6th threshold as seed points.

3.3 Enhancement filters

In this case we decided to apply in each volume the Frangi and OOF filters without any normalization step, first of all because we verified that the results were poorer comparing to the enhancement with the raw image, secondly because the filters are more robust to artifacts like the one we explained earlier.
On our data set we compared the optimal results of the two filters using a global threshold, and we verified that the OOF filters were better than the Frangi ones as you can see in Chapter 4. The method that we followed was to obtain the best global threshold on patient 70020; we then applied the results on the filtered volume of patient 63162.
In a second step we decided to build a classifier by using the features obtained from the OOF filter as it already gave us good results with a simple method like a global threshold. For the classification we used a Support Vector Machine (SVM), training 4 different models,
Before explaining what the SVM are it is important to understand that this method will give us a segmentation of the vessels, like the level set solution, but this is based on a different kind of approach. In fact, in the previous section, the goal was to find a solution of a cost function (see Chapter 2) that allowed as to find $\phi(t)$. In this case instead, we have to assign each voxels to two different categories by using a training set, where the categories of the voxels are known. To do so a classifier needs to be created by solving a minimization problem.
Many methods exist in the literature for such a task, and fall under the general term of *machine learning*. All these techniques are based on the idea that the computer learns

from a given training set of labelled observations, builds a model for the classification, then categorizes the observations of a new, unseen testing set.. In the next section you can see how this works for SVM and how we applied them in our work.

3.3.1 Support Vector Machines

Proposed in [13] the SVM have been widely used for many classification and regression problems. Over last years it has demonstrated to be a great solution in different areas; especially for medical image analysis (replacing well know methods like Neural Networks) for being quicker and easier to implement.
As we already said, the aim of this classifier is to learn a model from a training set, patient 70020, and then compute a prediction on the testing set (patient 63162). These sets were built by concatenating a vector of features M for each of the N observations to obtain a matrix with dimension $N \times M$. The best features are those which give strong discrimination between the two classes (vessel and background), so careful consideration is required when selecting the features to use. Our task is to categorise voxels as being within a vessel or part of the background, so the OOF filter, which was previously shown to give a strong response in vessels of different scales, was selected as a feature.
Given these pairs of features $\mathbf{x}$ and the respective classes $\mathbf{y} \in [-1; 1]$ where -1 is the background and 1 is the vessel, we have to search a linear separator with the maximum margin:

$$\min_{\mathbf{w}} \tfrac{1}{2} \|\mathbf{w}\| \quad with \quad y_i(\mathbf{w} \cdot \mathbf{x}_i + b) - 1 \geq 0 \quad \forall i = 1, \ldots, n \tag{3.2}$$

In Fig.3.6 we can see the margin between the classes defining two different hyperplanes

were the observations will be projected. The red line represent the separator at $\mathbf{w} \cdot \mathbf{x}_i + b = 0$ so the margin $2r$ is equal to:

$$r = \frac{y_i(\mathbf{w} \cdot \mathbf{x}_i + b)}{2 \|\mathbf{w}\|} \tag{3.3}$$

In Eq.3.2the primal problem of SVM is showed. The solution at this point can already be found already, but with a very high computational cost. In order to be more efficient the problem must be evaluated to the dual formulation by firstly constraining the cost function, using the Lagrange multipliers a_i:

$$L(\mathbf{w}, b, a) = \tfrac{1}{2} \|w\|^2 - \textstyle\sum_{i=1}^{n} a_i y_i (\mathbf{w} \cdot \mathbf{x}_i + b)$$

$$\max_{b,a} \min_{w} L(\mathbf{w}, b, a) \tag{3.4}$$

This extension of Lagrange multipliers method is also called the *Kuhn-Tucker theorem*. By the evaluation of $\frac{\partial L(\mathbf{w},b,a)}{\partial \mathbf{w}}$, that gives $\mathbf{w} = \sum_{i=1}^{n} a_i y_i x_i$, is then possible to express the minimization problem in the dual form as:

$$\max_{a} \textstyle\sum_{i=1}^{n} a_i - \tfrac{1}{2} \sum_{i=1}^{n} \sum_{j=1}^{n} a_i a_j y_i y_j (\mathbf{x}_i \cdot \mathbf{x}_j)$$

$$where\ a_i \geq 0 \qquad and\ \textstyle\sum_{i=1}^{n} a_i y_i \tag{3.5}$$

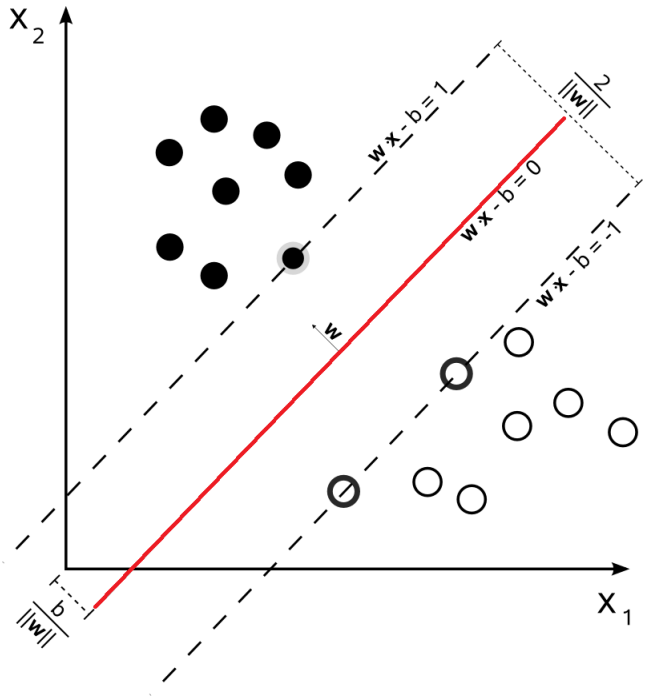

Figure 3.5: Margin for classification

It's then easy to notice that:

$$a_i > 0 \leftrightarrow y_i(\mathbf{w}_i \cdot \mathbf{x}_i) = 1 \tag{3.6}$$

these vectors are called *support vectors*. By expressing $y(\mathbf{X}) = \sum_{i=1}^{n} a_i y_i \mathbf{X}_i \cdot \mathbf{X} + b$, we can memorize only the SV $\mathbf{X_s} \in S$ for the classification of new examples.
In order to control the sensitivity of the SVM to *outliers*, a *slack* variable ξ_i is then introduced. This new tuning element changes the cost function as:

$$\min_{\mathbf{w}} \tfrac{1}{2} \|\mathbf{w}\| + C \sum_{i=1}^{n} \xi_i$$

$$y_i(\mathbf{w} \cdot \mathbf{x}_i + b) \geq 1 - \xi_i$$

$$\xi_i \geq 0 \tag{3.7}$$

This is now called *soft margin*. The slackness is defined by the value of ξ_i, so if $1 \geq \xi_i \geq 0$ the data will be situated between the margin line and the correct side of the hyperplane, instead $\xi_i \geq 1$ implies that the observation will be misclassified. Notice that there is another parameter C that can control the effect of the soft margin: if it is close to 0 we create a wide region that does not heavily weight the misclassified points, whereas a very high value for C tends towards the hard margin problem described in Eq.3.2.
Finally, we must address the Cover Theorem, which says :

> *A complex pattern-classification problem, cast in a high-dimensional space nonlinearly, is more likely to be linearly separable than in a low-dimensional space, provided that the space is not densely populated.*

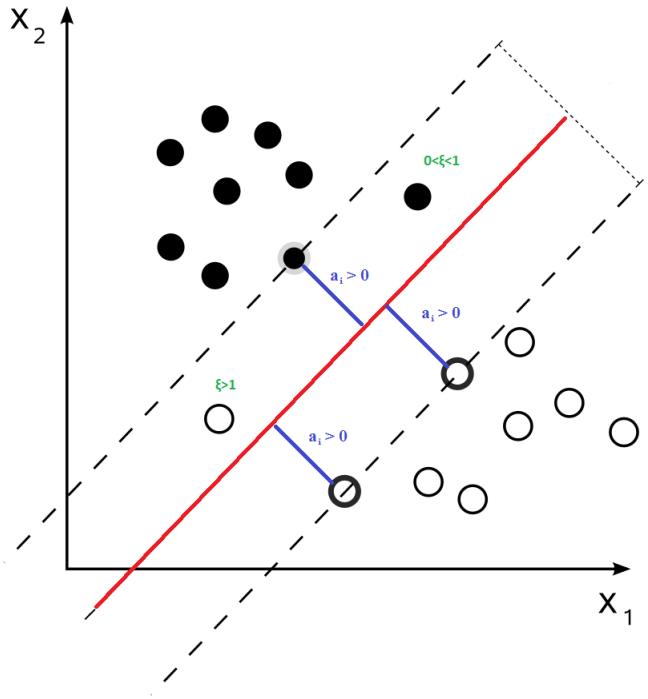

Figure 3.6: Lagrange multipliers and slacks

Our dual form will change as:

$$\max_a \sum_{i=1}^{n} a_i - \frac{1}{2} \sum_{i=1}^{n} \sum_{j=1}^{n} a_i a_j y_i y_j (\phi(\mathbf{x}_i) \cdot \phi(\mathbf{x}_j))$$

$$C \geq a_i \geq 0 \tag{3.8}$$

where you can see the mapping function $\phi()$ and the constraint on a due to the introduction of the slacks.
The disadvantage this expression encounters is that the computation of the $\phi(\mathbf{x})$ for each data has a very high computational cost, nevertheless we are only interested in the computation of the scalar product between the two function in Eq.3.8.
To evaluate this product we then introduce the concept of Kernel, that is each function $K(\mathbf{x}_i, \mathbf{x}_j)$ which has, as results, a $N^{n \times n}$ positive semi-definite matrix. This function can be computed directly on $\mathbf{x}$, and in our study we decided to use the one called RBF (Radial Basis Function),with the following expression:

$$K(\mathbf{x}_i, \mathbf{x}_j) = e^{-\gamma \|\mathbf{x}_i - \mathbf{x}_j\|^2} \tag{3.9}$$

where γ must be set up during the training.
In the last two paragraphs we will discuss firstly how to select the user parameters γ and C, then how we decided to create a data set for the training and how we treated the imbalance between the two classes.

Setting of γ, C and weights

Setting C and γ correctly is a very delicate step to obtain the best classification with SVMs. In particular, once a data set is given, we have on the one hand to obtain the

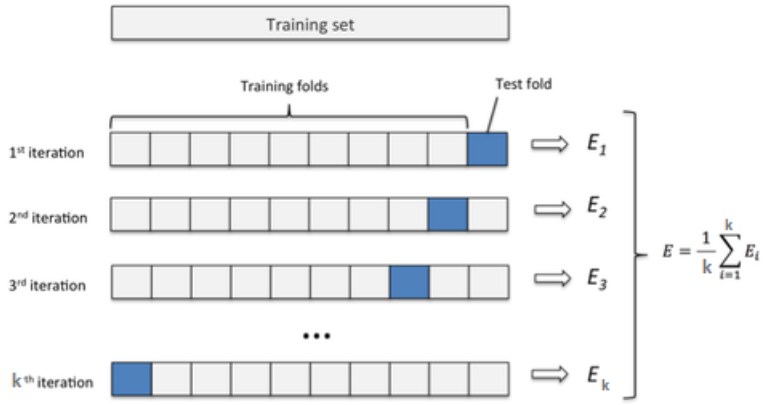

Figure 3.7: K-fold cross validation

best classification ((i.e. segmentation)) of the training set, but, on the other hand, we need to avoid over-fitting that can cause bad results on the testing set.
A well-known method to tune these parameters without falling in over fitting is the *k-folds cross validation*. This solution is based on the partition of the data set in k different folds: the next steps are to perform the training on $k-1$ folds and then to test on the remaining fold. In our study the value of k is fixed to 4 in both station 1 and 2, then $k = 6$ is chosen for station 3 and 4. The results of the test were evaluated with DICE coefficient and averaged for each fold. We choose for each station the pair that gave us the best segmentation score by performing a 2D grid search with $C$and γ.

During the computation of the model we have also to consider that the two classes are strongly unbalanced, for example in station 3 the percentage of vessels voxels is around the 0.3%. In order to overcome this obstacle is necessary to weight the classification during the training:

$$w_1 = \frac{N}{2N_1} \quad w_2 = \frac{N}{2N_2} \tag{3.10}$$

where $N = N_1 + N_2$ is the dimension of the training set, N_1 and N_2 are the dimensions of the two classes.
Another issue that we encountered was the composition of the raw volumes. We noticed that the majority of the voxels were at low intensity levels (as most of the angiography images) and we considered that, by the evaluation of the complete data set, we would have lost some discriminative power in the minimization of the Eq.3.8. Moreover the computational cost of the training and testing would have been too high if we had to use the voxels with a value near zero.

Testing and training set We considered that the real discrimination of voxels that the SVM would have done, was around the vessels. In particular we hypothesise that by taking a neighborhood of the ground truth, we could have a model that could operate the classification on the most critical voxels, so the segmentation would have been more clear and accurate. By using a 3D dilation operator and a random selection of 20000 voxel in the volume we created our *neighbors training set*. The testing set (pa-

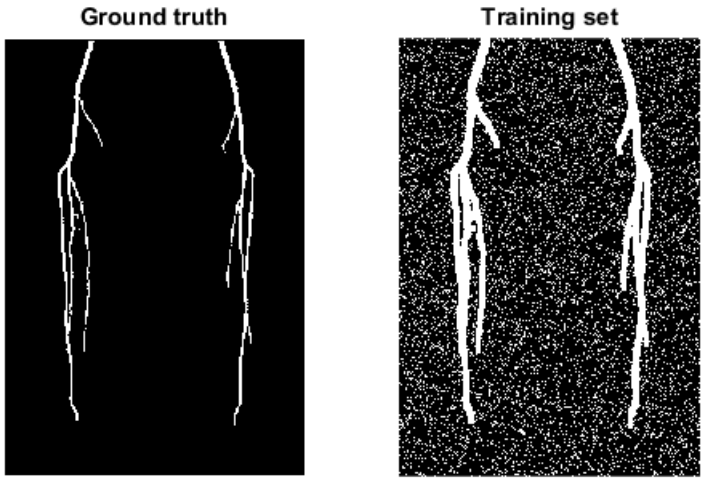

Figure 3.8: Training set example of station 4

tient 63162), was constructed by applying a soft threshold on each station (given by $Max_{intensity}/20$), discarding the lowest intensity voxels which are guaranteed to not be part of a vessel. This was verified in practice, where it was found that no true vessel voxels were discarded.

CHAPTER

4

RESULTS

In this chapter we present the results achieved when applying the algorithms described in Chapter 3 to our patient datasets.

4.1 Station 1

As can be seen in the raw data of Figure 4.2, the subtraction process in this station leaves many high intensity regions which are not arteries of interest for this study (particularly around the heart and lungs), and therefore not included in the ground truth segmentation set. For this reason, even if the segmentation is very accurate in the other parts of the thorax, we expect a lower score comparing to the other stations.

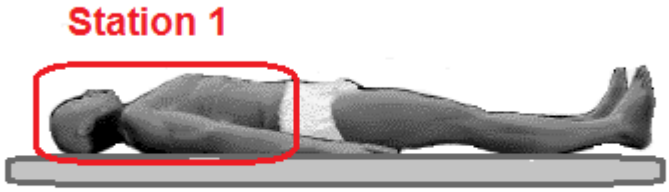

Figure 4.1: Station 1 scan

4.1.1 Level set

Fig. 4.2 shows the smoothing applied to the *local vessel intensity* of the volume.

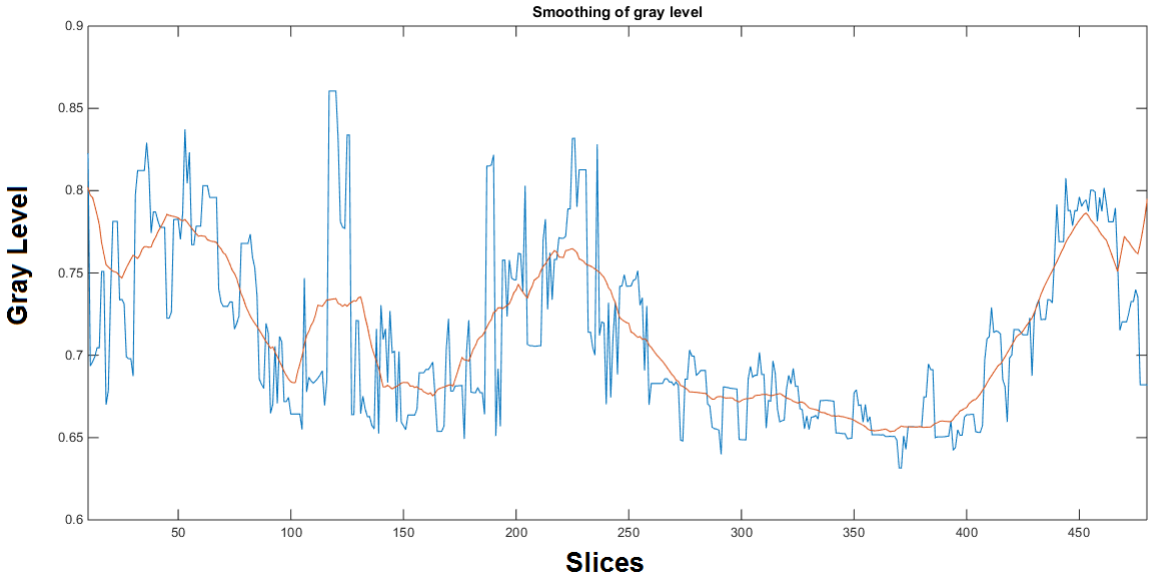

Figure 4.2: Smoothing of station 1

In Fig. 4.3 instead you can see the normalization and the level set are displayed.

4.1.2 Threshold on Frangi and OOF

The results of this section were obtained with the following setting:

Frangi in Fig 4.4

- Scale factor: [1 2 3 4 5 6 8 9 10 11 12 13 14 15]
- α and β: 0.5

OOF in Fig 4.5

- Radii: [1 2 3 4 5 6 8 9 10 11 12 13 14 15]
- σ: 0.4

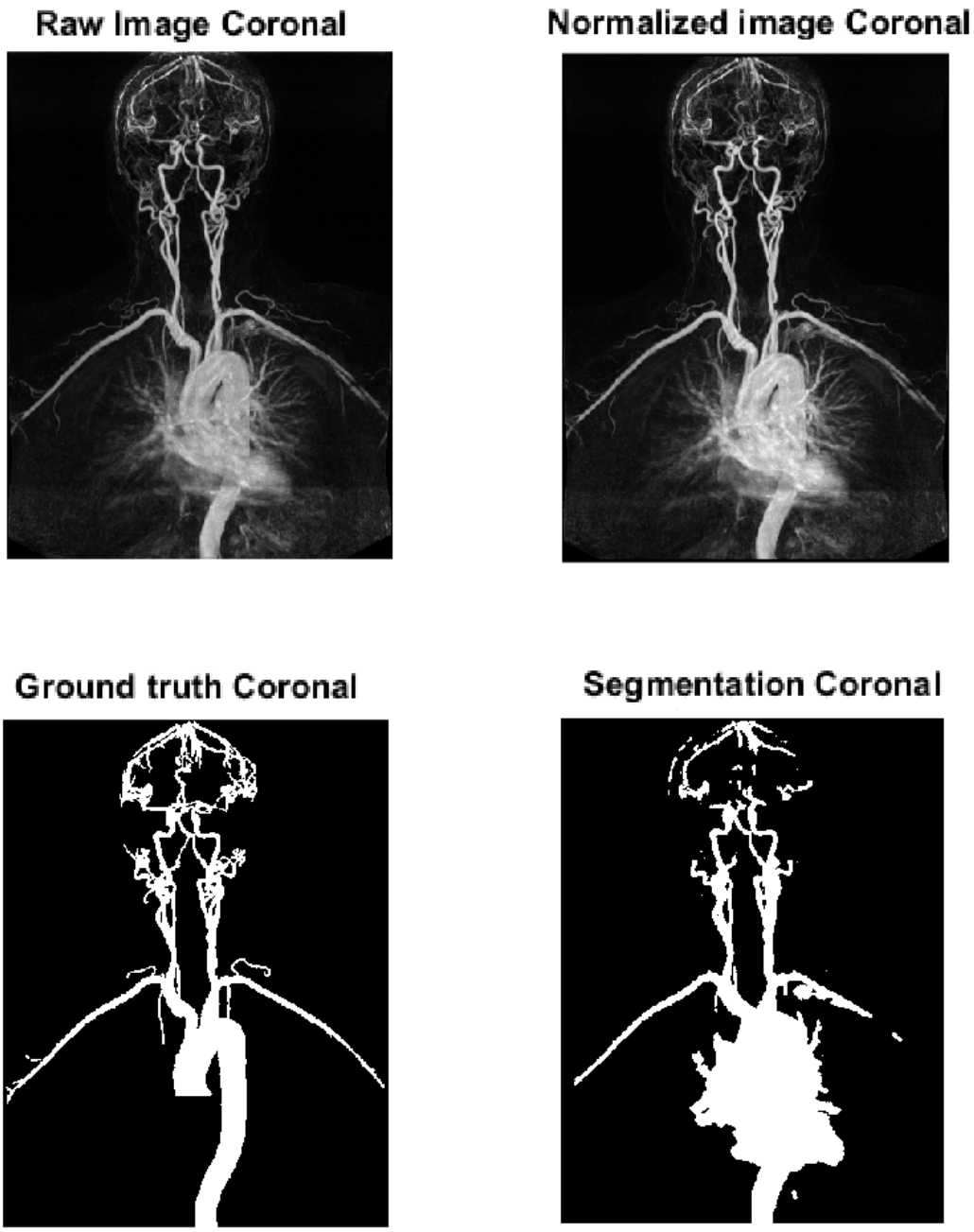

Figure 4.3: Level set result: in the top-left you can see the raw image, in the top-right the normalized image, in the bottom-left the ground truth segmentation and finally in the bottom-right the level set

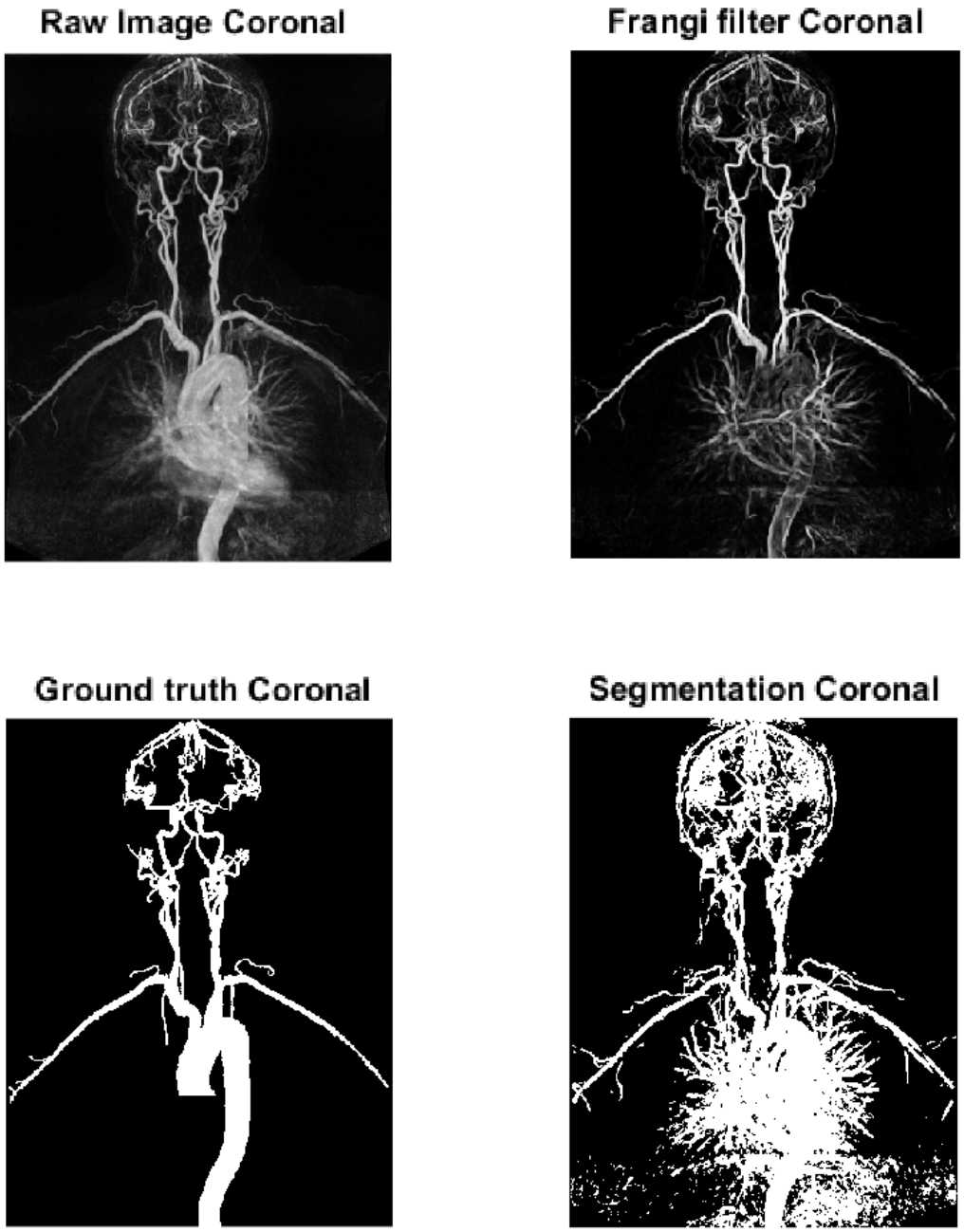

Figure 4.4: Frangi enhancement and segmentation: in the top-left you can see the raw image, in the top-right the filtered image, bottom-left the ground truth and in bottom-right the final segmentation result

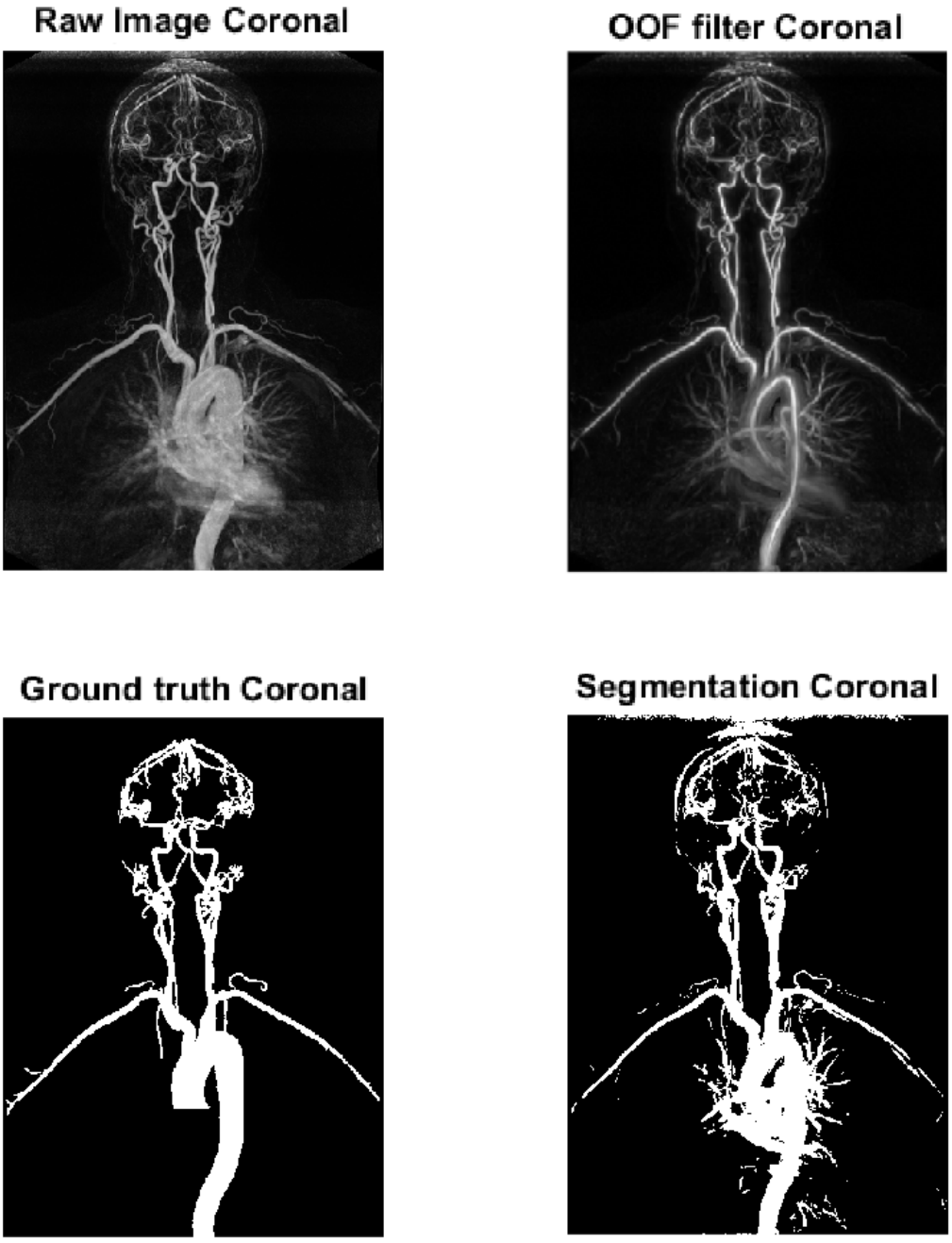

Figure 4.5: OOF enhancement and segmentation: in the top-left you can see the raw image, in the top-right the filtered image, bottom-left the ground truth and in bottom-right the final segmentation result

4.1.3 SVM

The 4-fold cross validation has determined that the best parameters for the settings of the SVM were:

- γ: 0.0183
- C: 7.3891

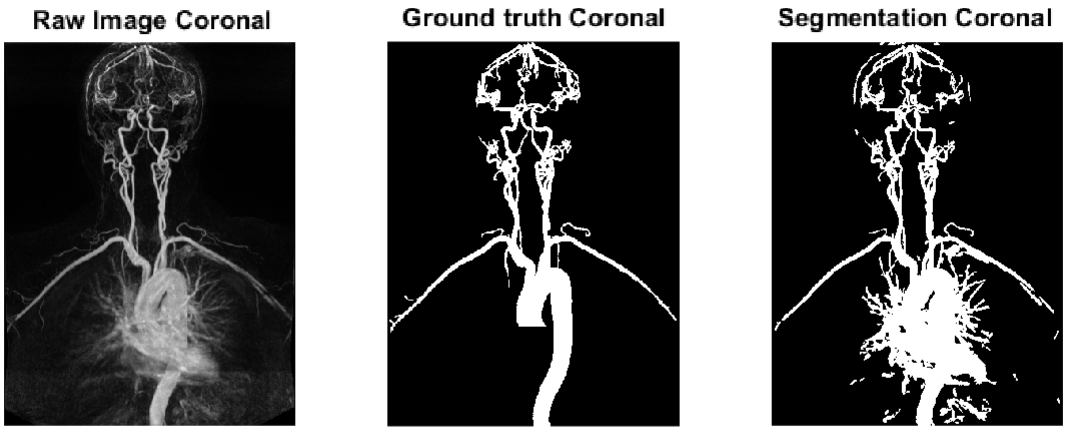

Figure 4.6: Segmentation with SVM

4.2 Results

Table 1 shows the final DSC results for Station 1:

Method	Level set	Frangi + thresh	OOF + Thresh	OOF + SVM
DSC	0.457	0.394	0.529	0.587

Table 4.1: Dice coefficient results for Station 1

In order to consider the fact that it is almost impossible for each method to avoid the selection of the pulmonary vessel we try to evaluate the DICE score without V_{lungs} as in Fig. For example the DICE score of SVM segmentation increased to almost 0.827.

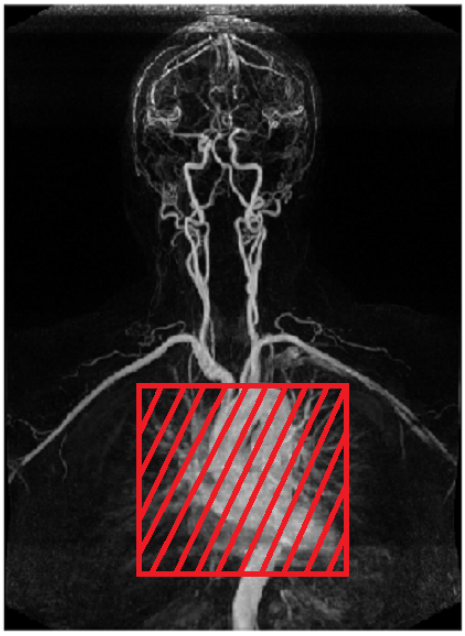

Figure 4.7: Lungs have discharged

4.3 Station 2

In this station, as you can see from the next figures, the critical segmentation task is to avoid the abdominal organs not removed by the subtraction process, particularly the kidneys. Thanks to the fact that the seeds point for the level set are usually at an higher gray level than the one in the kidneys and by the properties of the OOF and Frangi filters we expect a good classification of the volumes.

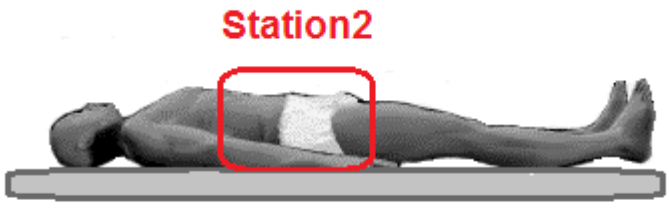

Figure 4.8: Station 2 scan

4.3.1 Level set

Fig. 4.9 shows the smoothing applied to the *local vessel intensity* of the volume.

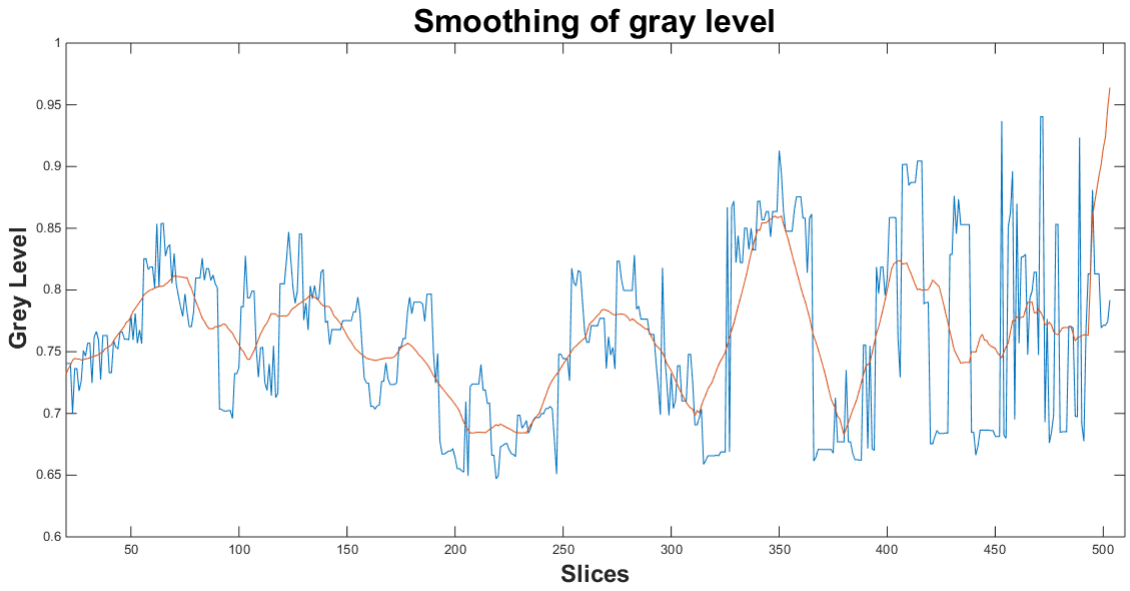

Figure 4.9: Smoothing of station 2

In Fig. 4.10 instead you can see the normalization and the level set are displayed.

4.3.2 Threshold on Frangi and OOF

The results of this section were obtained with the following setting:

Frangi in Fig 4.11

- Scale factor: [1 2 3 4 5 6 7 : 8 9 10]
- α and β: 0.5

OOF in Fig 4.12

- Radii: [1 2 3 4 5 6 7 : 8 9 10]
- σ: 0.5

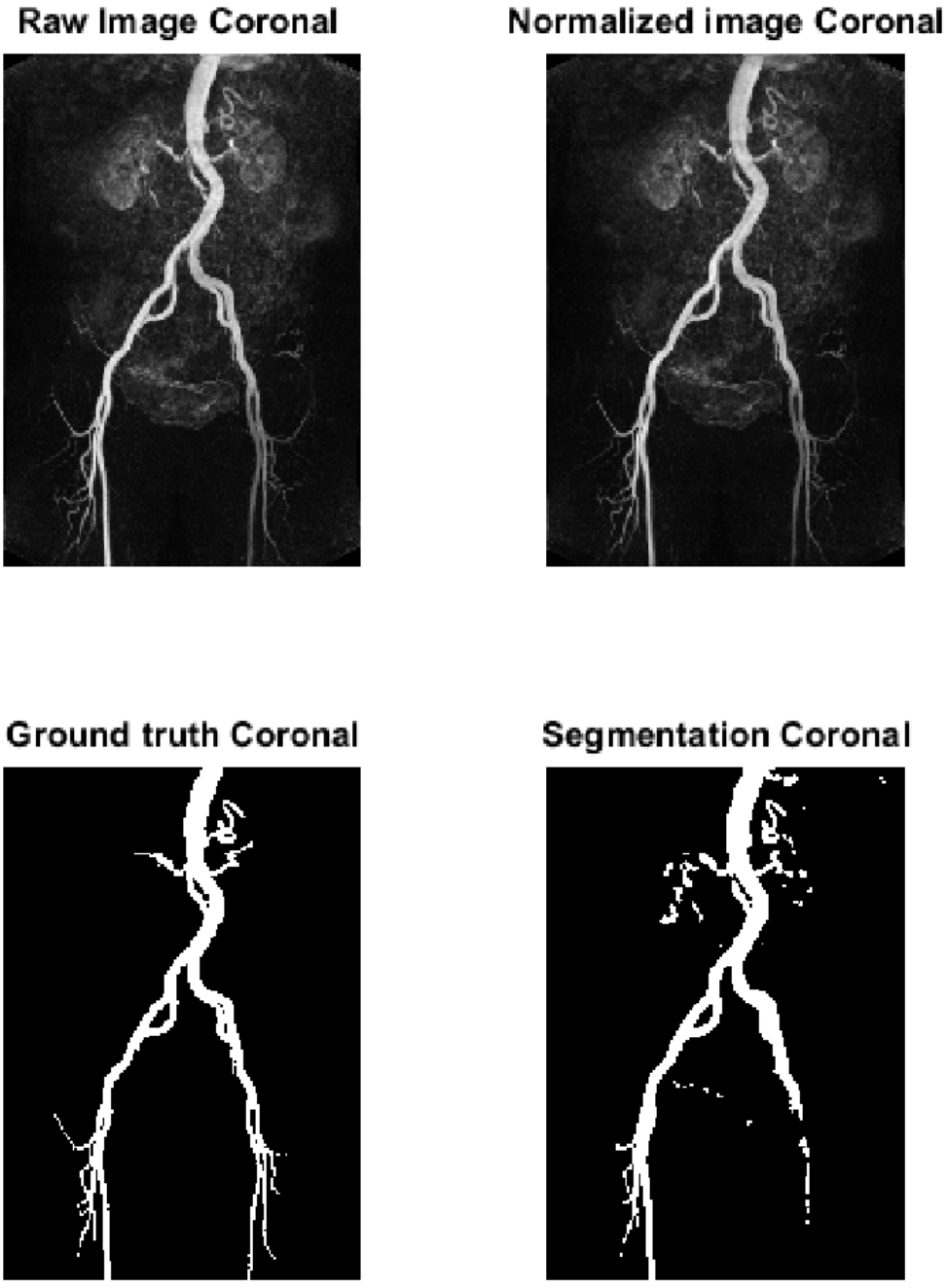

Figure 4.10: Level set result: in the top-left you can see the raw image, in the top-right the normalized image, in the bottom-left the ground truth segmentation and finally in the bottom-right the level set

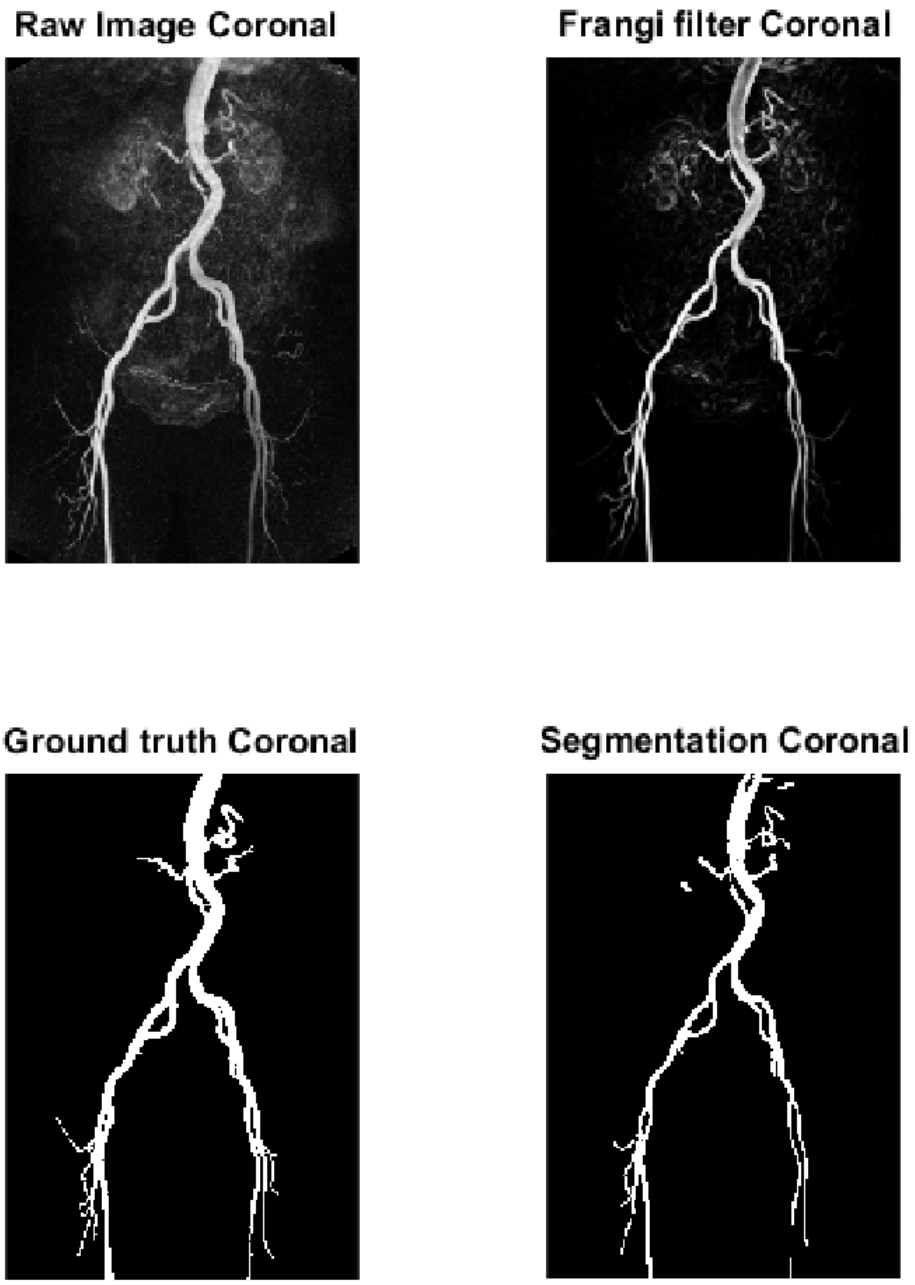

Figure 4.11: Frangi enhancement and segmentation: in the top-left you can see the raw image, in the top-right the filtered image, bottom-left the ground truth and in bottom-right the final segmentation result

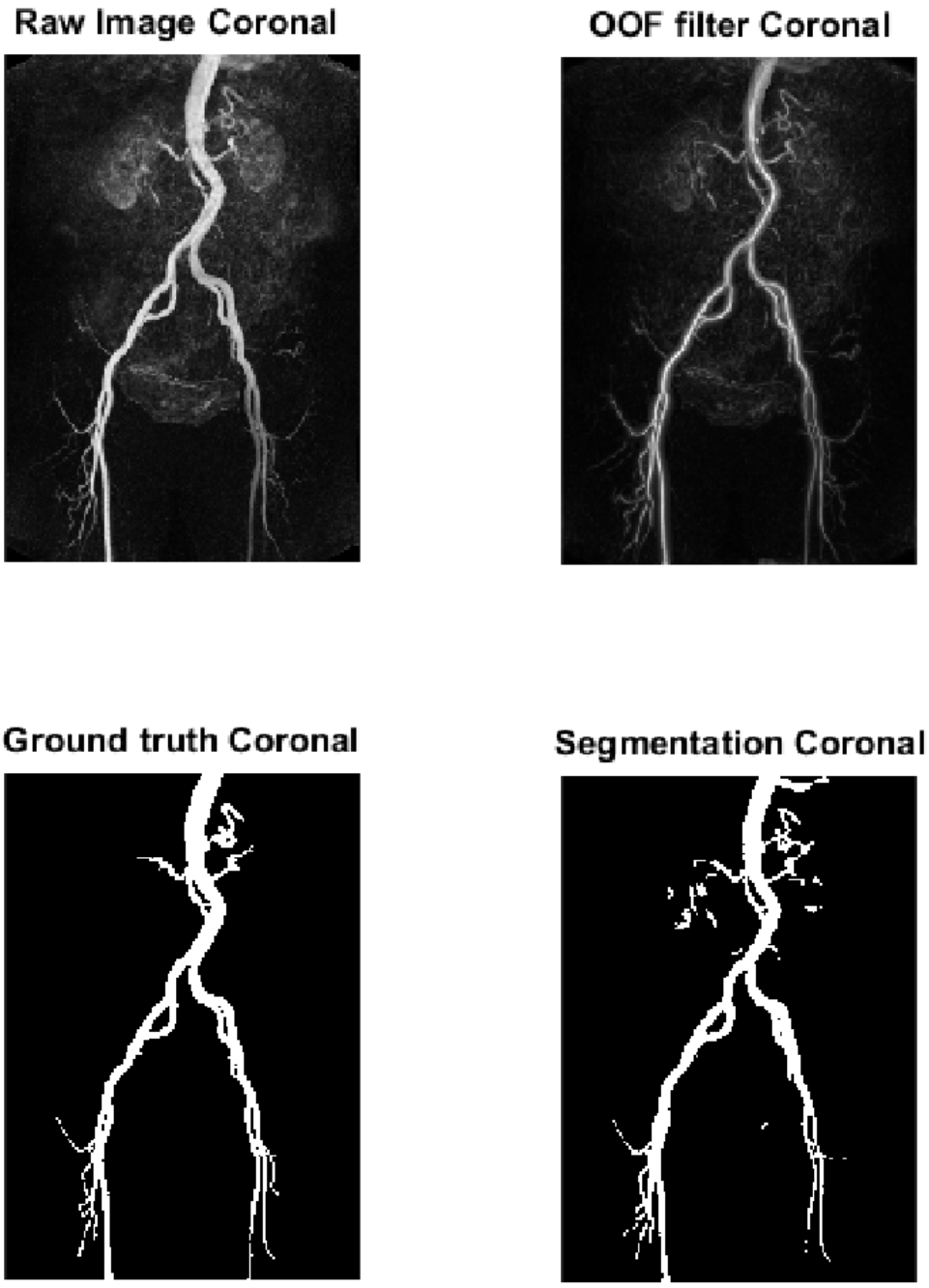

Figure 4.12: OOF enhancement and segmentation: in the top-left you can see the raw image, in the top-right the filtered image, bottom-left the ground truth and in bottom-right the final segmentation result

4.3.3 SVM

The 4-fold cross validation has determined that the best parameters for the settings of the SVM were:

- γ: 0.0067
- C: 7.3891

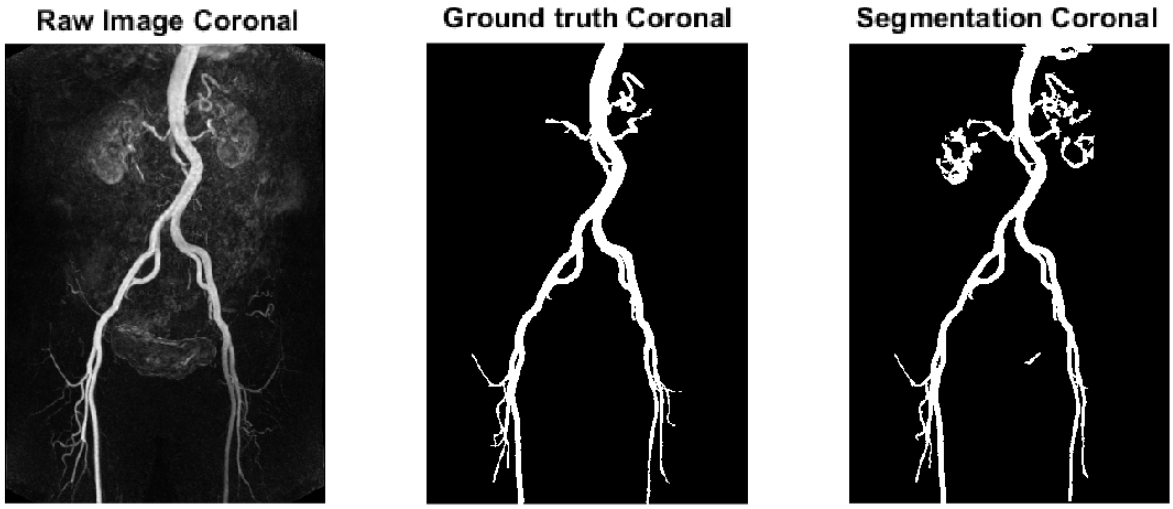

Figure 4.13: Segmentation with SVM

4.4 Results

Table 2 shows the final DSC results for Station 2:

Method	Level set	Frangi + thresh	OOF + Thresh	OOF + SVM
DSC	0.83073	0.6735	0.7773	0.8062

Table 4.2: Dice coefficient results for Station 2

Notice that in Fig.4.13 the kidney segmentation is highly fragmented while the arteries seem to be full connected. By a simple step of post-processing we can extract the arteries structures by taking only the connected components like in Fig.4.14. The results is a DICE coefficient that can increase to 0.8501.
Nevertheless we have to be very careful with this post-processing step because when in an healthy patient it can be useful, in a patient that suffers from stenosis there is the

chance to discard arteries that are non connected, but are very important for calibre measurement.

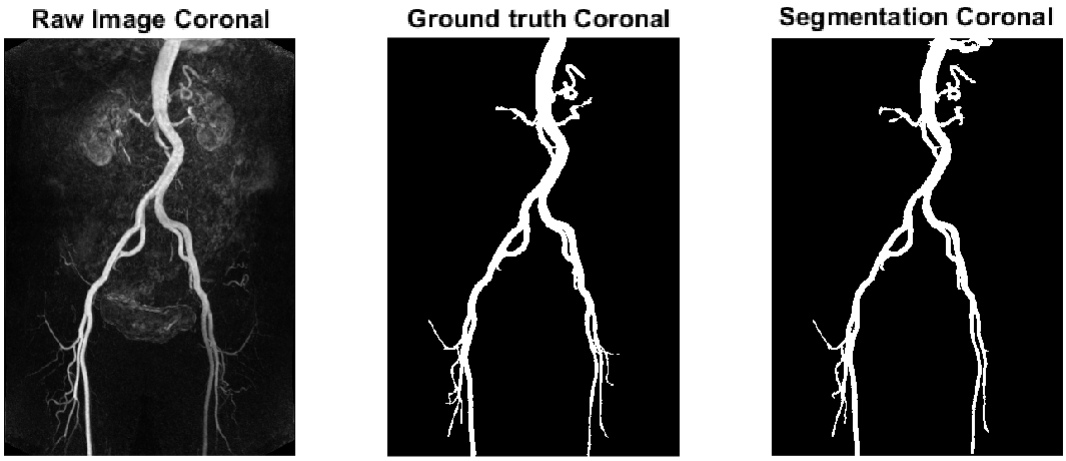

Figure 4.14: Connected components from SVM classification

4.5 Station 3

The legs are a very interesting area for clinicians. The main vessels that are descending from the hip along the thigh are called *femoral arteries* and are often one of the main sites of arterial narrowing on unhealthy patient.
In our analysis we find out that this station suffers from artifacts due to recirculation of tracer inside the veins, so the task of extracting only the arteries is very challenging especially in the upper part. For this reason we decided to change the minimum scale and ratio for the filters in order to be more selective on the smaller vessel (usually veins). The seed point of the levels set, on contrary, are more robust to this artifact thanks to the fact that they are more brighter than the voxels in the veins.

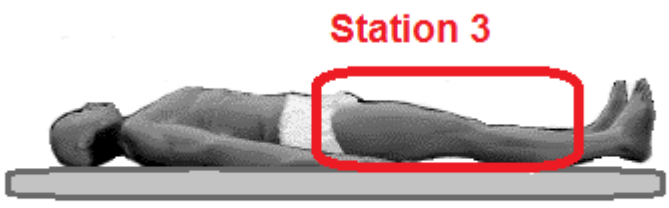

Figure 4.15: Station 3 scan

4.5.1 Level set

Fig. 4.16 shows the smoothing applied to the *local vessel intensity* of the volume.

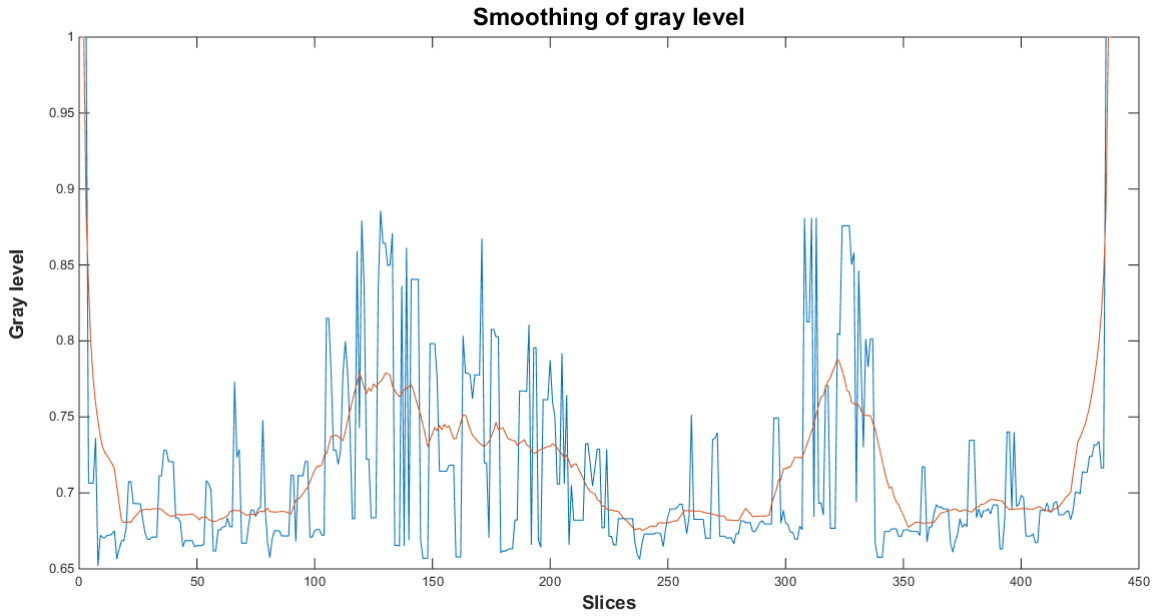

Figure 4.16: Smoothing of station 3

In Fig. 4.17 instead you can see the normalization and the level set are displayed.

4.5.2 Threshold on Frangi and OOF

The results of this section were obtained with the following setting:

Frangi in Fig 4.18

- Scale factor: [3 3.25 3.5 3.75 4 4.25 4.5 : 4.75]
- α and β: 0.5

OOF in Fig 4.19

- Radii: [3 3.25 3.5 3.75 4 4.25 4.5 : 4.75]
- σ: 0.5

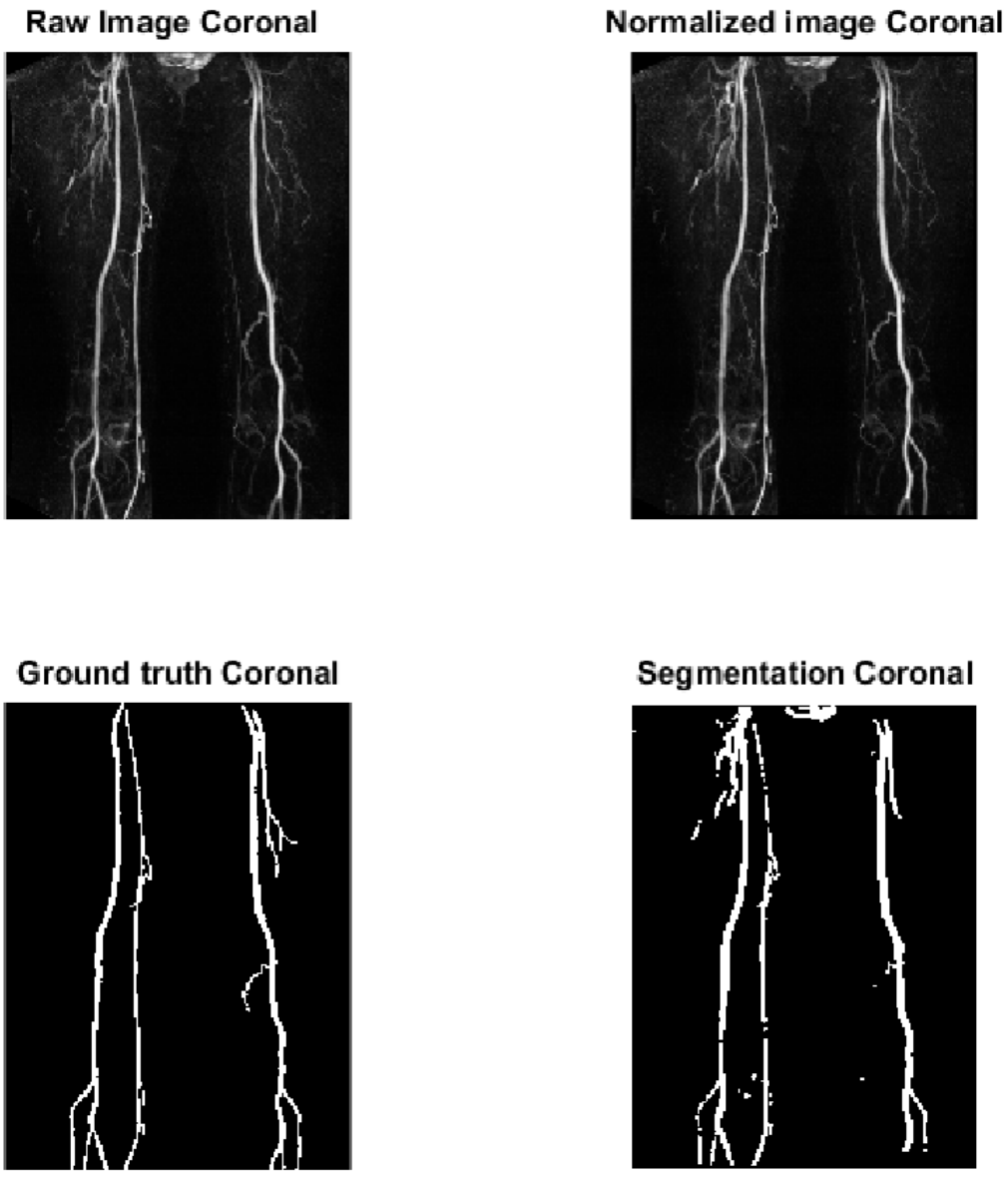

Figure 4.17: Level set result: in the top-left you can see the raw image, in the top-right the normalized image, in the bottom-left the ground truth segmentation and finally in the bottom-right the level set

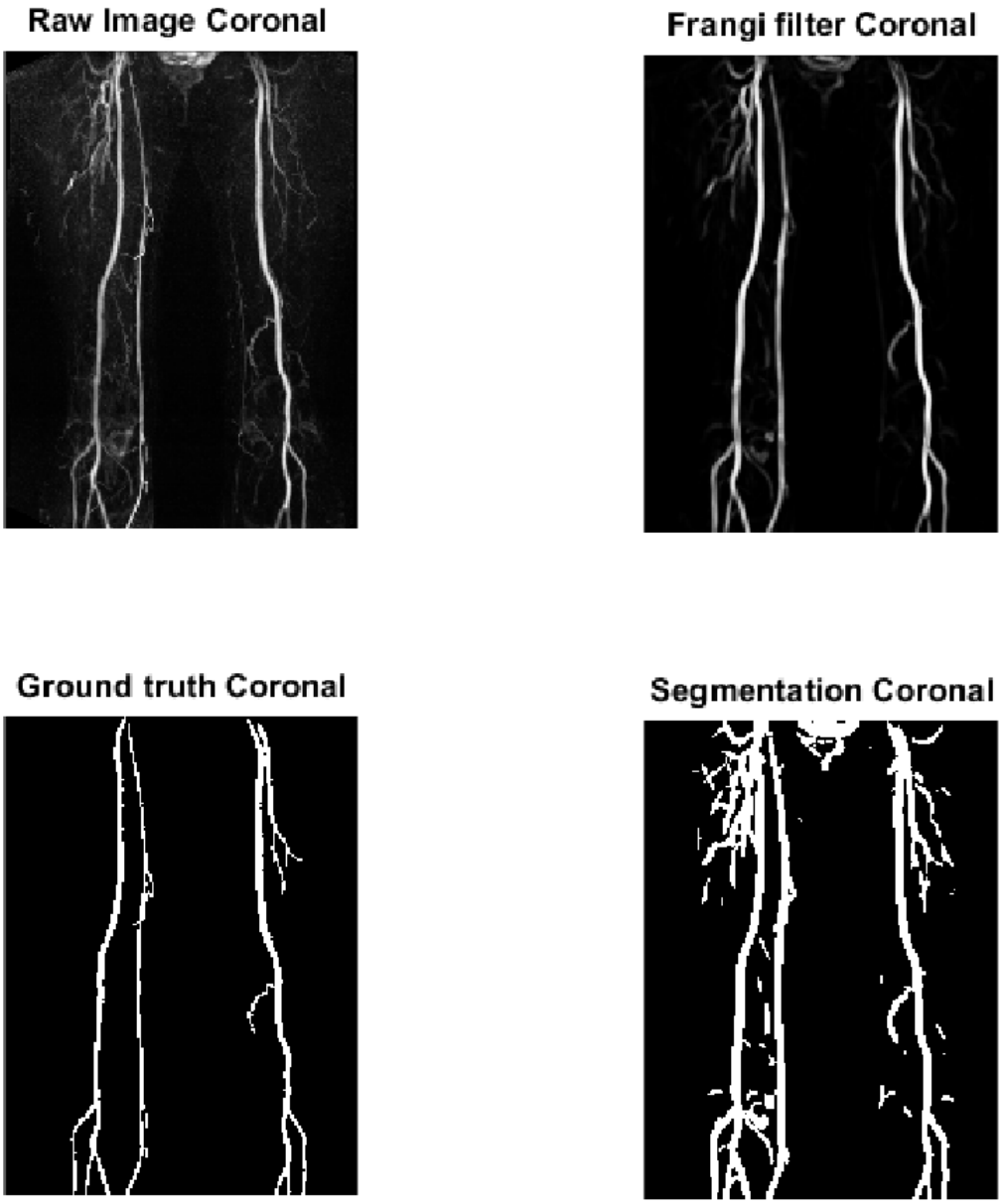

Figure 4.18: Frangi enhancement and segmentation: in the top-left you can see the raw image, in the top-right the filtered image, bottom-left the ground truth and in bottom-right the final segmentation result

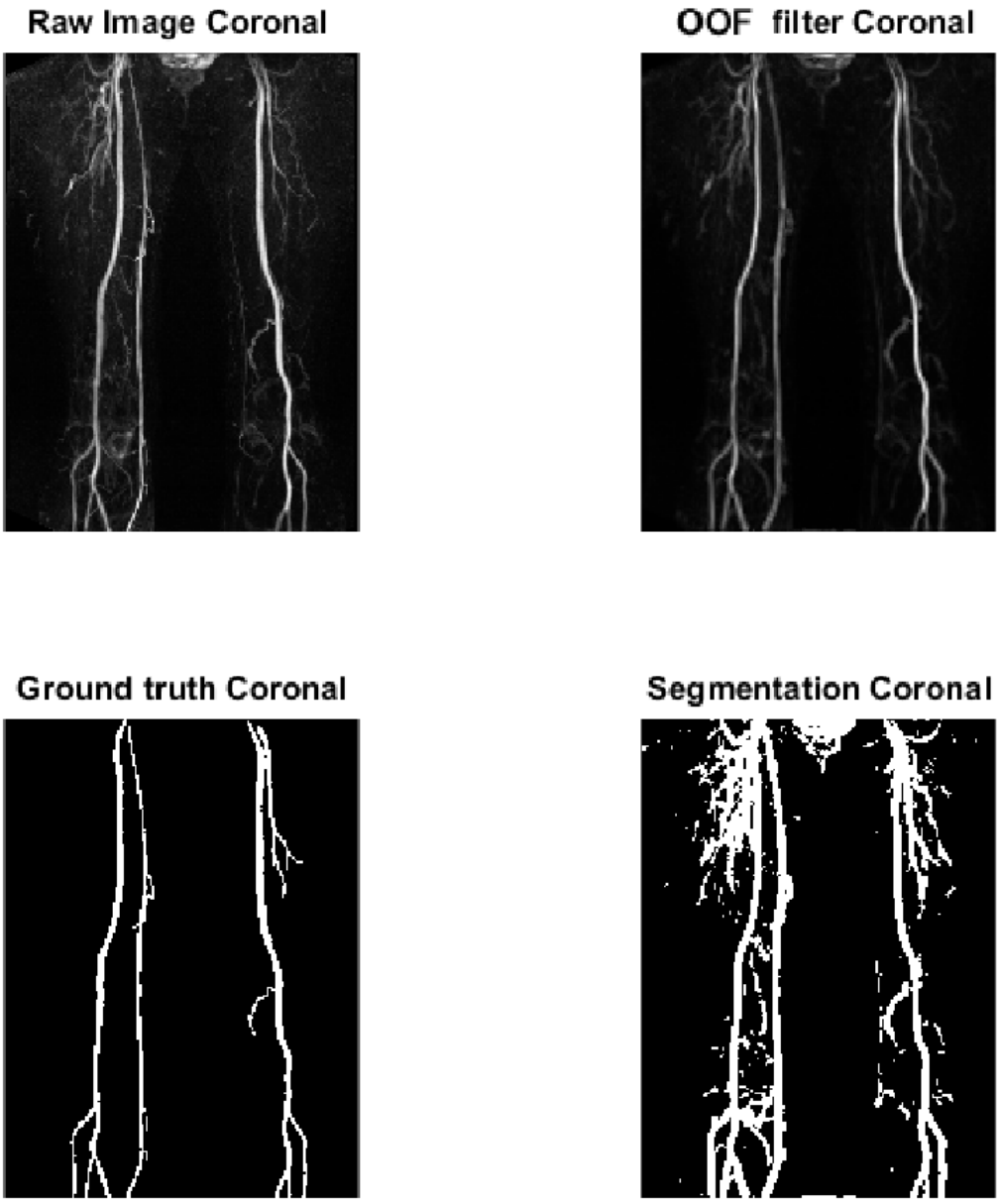

Figure 4.19: OOF enhancement and segmentation: in the top-left you can see the raw image, in the top-right the filtered image, bottom-left the ground truth and in bottom-right the final segmentation result

4.5.3 SVM

The 6-fold cross validation has determined that the best parameters for the settings of the SVM were:

- γ: 0.0025
- C: 20.0855

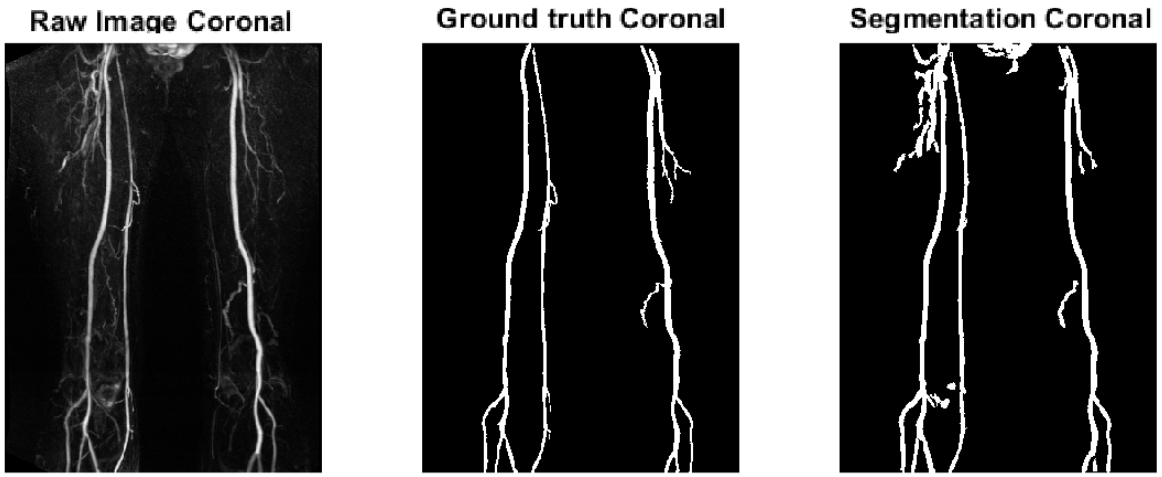

Figure 4.20: Segmentation with SVM

4.6 Results

Table 3 shows the final DSC results for Station 3:

Method	Level set	Frangi + thresh	OOF + Thresh	OOF + SVM
DSC	0.7214	0.4528	0.5109	0.714

Table 4.3: Dice coefficient results for Station 3

It can be seen that the non-arterial vessel structures present in this station (Figure 4.21) pose a significant challenge to the vesselness-filter approaches. Additional post-processing may help correct these issues, but exploring such solutions was beyond the scope of this work.

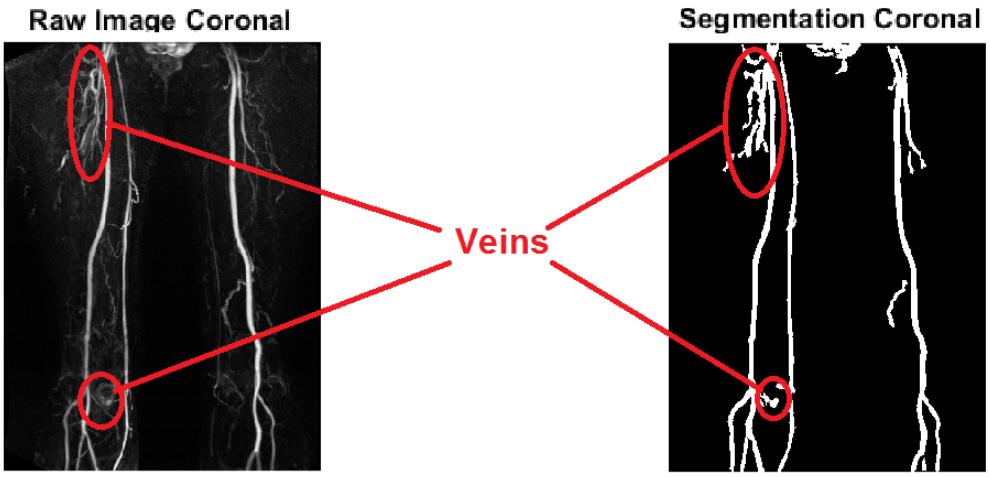

Figure 4.21: Veins artifact on the legs

4.7 Station 4

This is the station that, in our work, was less subjected by the artifacts and it did not require an important post-processing step. In the next figures you will see that the behavior of each model is quite good, especially for the SVM classifier.

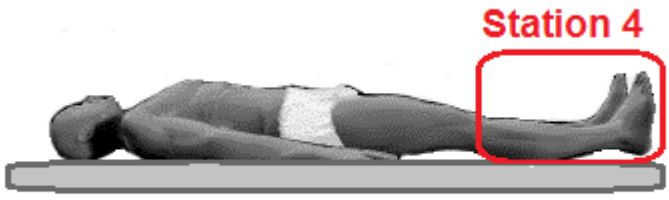

Figure 4.22: Station 4 scan

4.7.1 Level set

Fig. 4.23 shows the smoothing applied to the *local vessel intensity* of the volume.

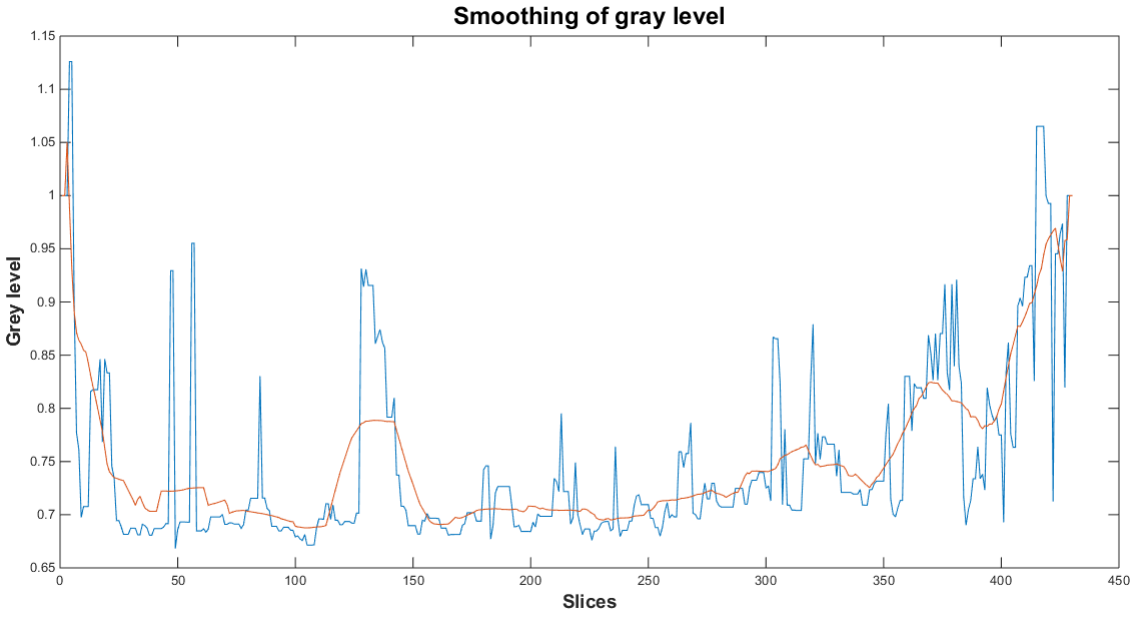

Figure 4.23: Smoothing of station 4

In Fig. 4.24 instead you can see the normalization and the level set are displayed.

4.7.2 Threshold on Frangi and OOF

The results of this section were obtained with the following setting:

Frangi in Fig 4.25

- Scale factor: [1 0.5 2 2.5 3 3.5 4]
- α and β: 0.5

OOF in Fig 4.26

- Radii: [1 0.5 2 2.5 3 3.5 4]
- σ: 0.4

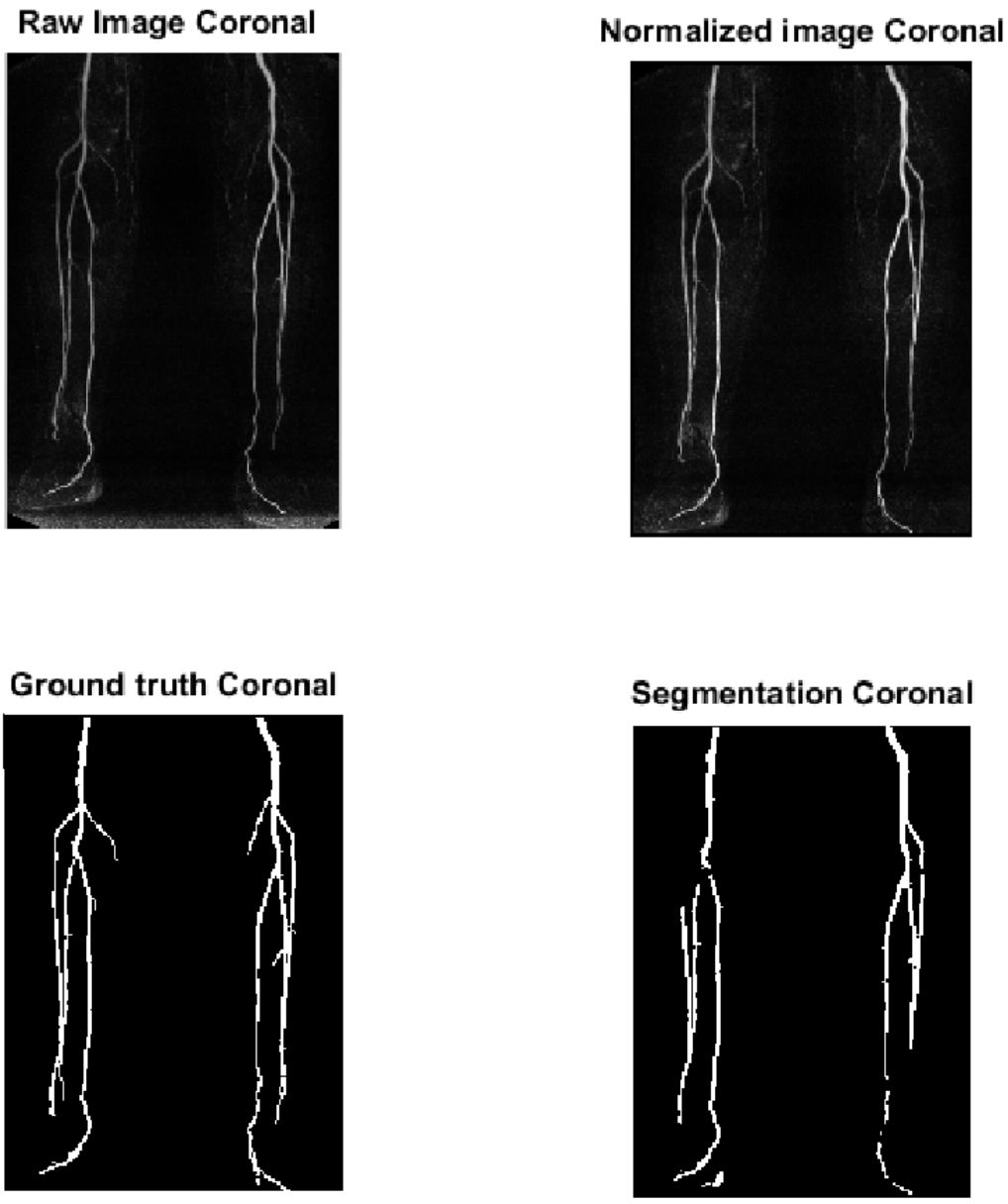

Figure 4.24: Level set result: in the top-left you can see the raw image, in the top-right the normalized image, in the bottom-left the ground truth segmentation and finally in the bottom-right the level set

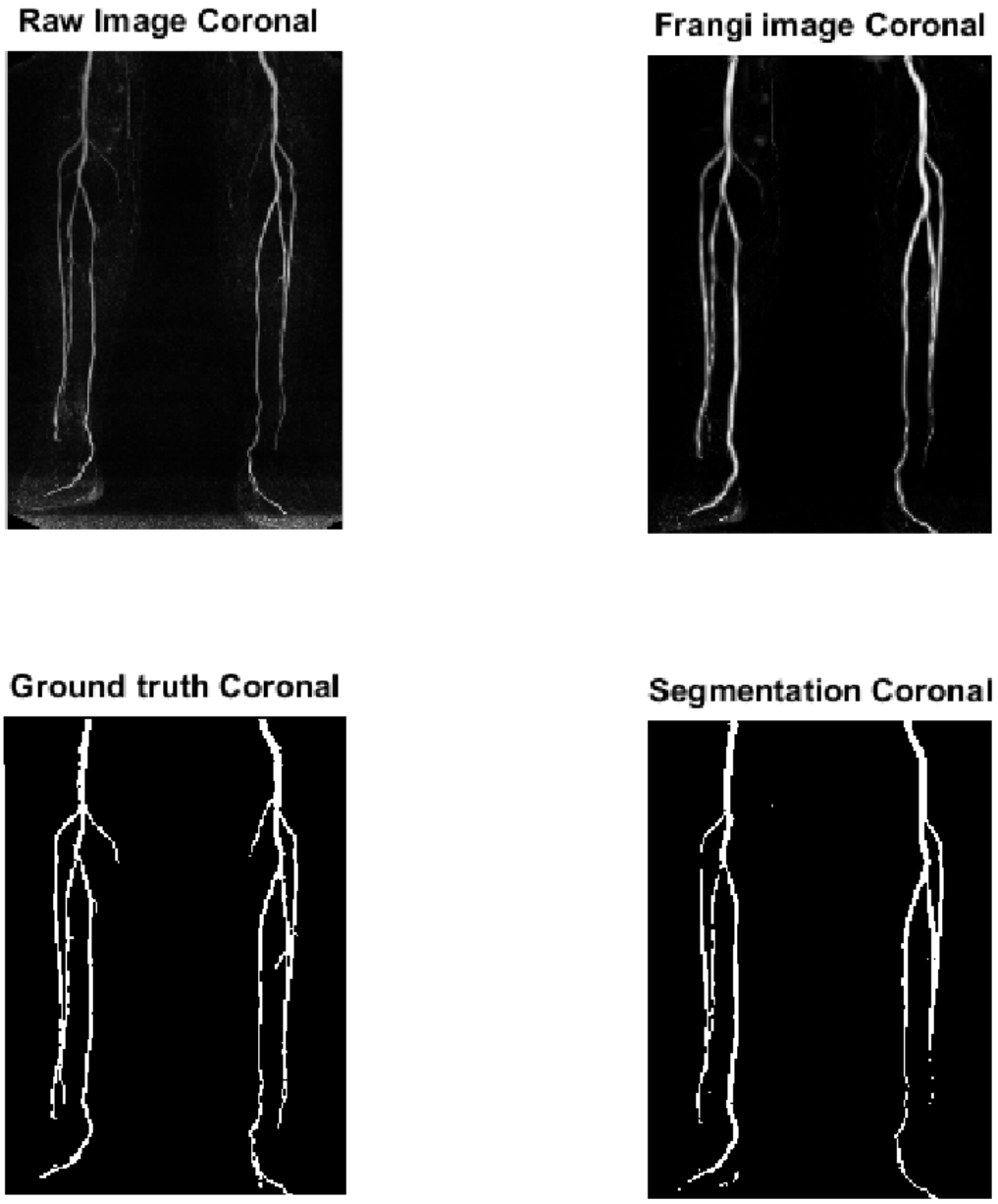

Figure 4.25: Frangi enhancement and segmentation: in the top-left you can see the raw image, in the top-right the filtered image, bottom-left the ground truth and in bottom-right the final segmentation result

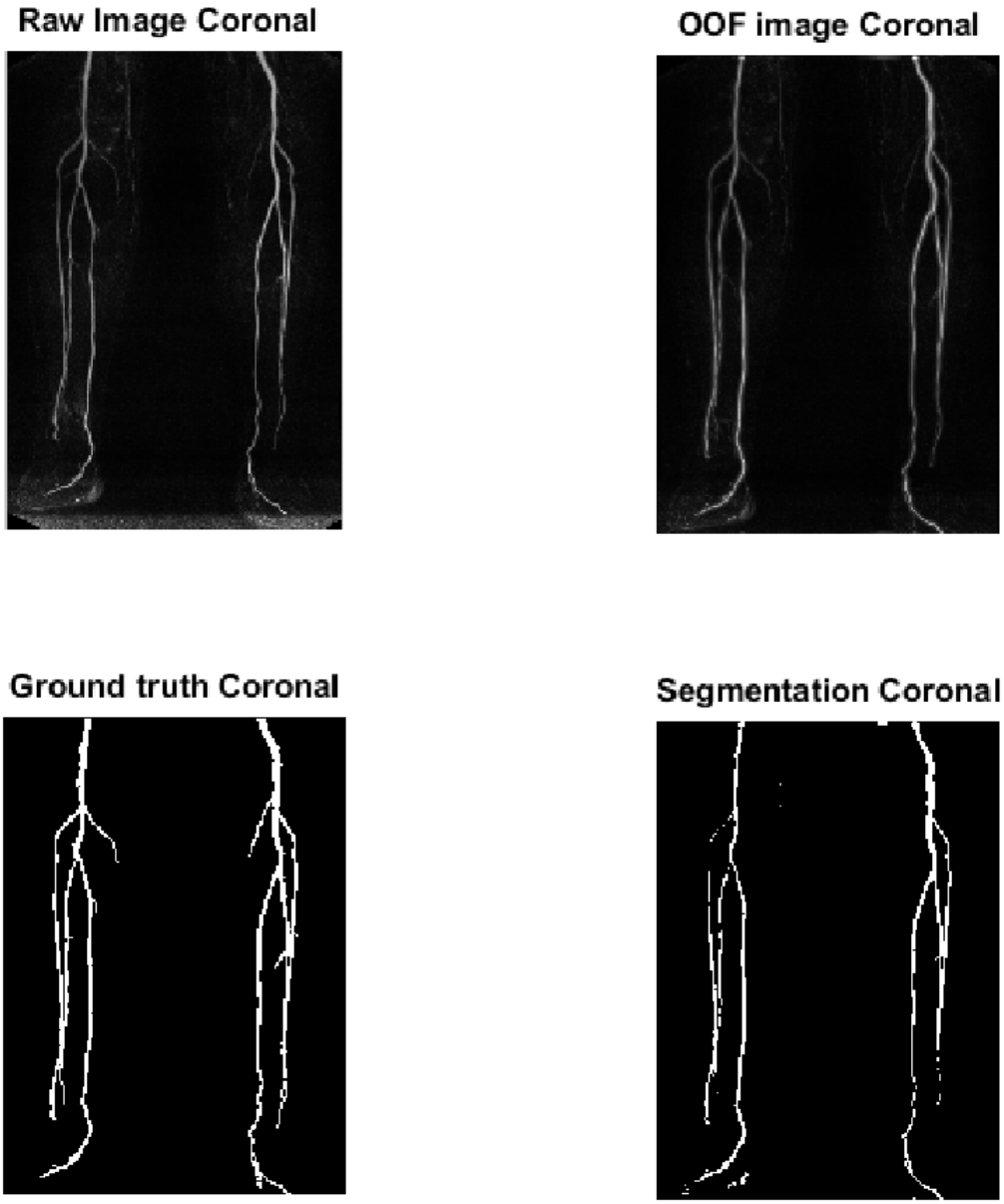

Figure 4.26: OOF enhancement and segmentation: in the top-left you can see the raw image, in the top-right the filtered image, bottom-left the ground truth and in bottom-right the final segmentation result

4.7.3 SVM

The 6-fold cross validation has determined that the best parameters for the settings of the SVM were:

- γ: 0.1353
- C: 2.7183

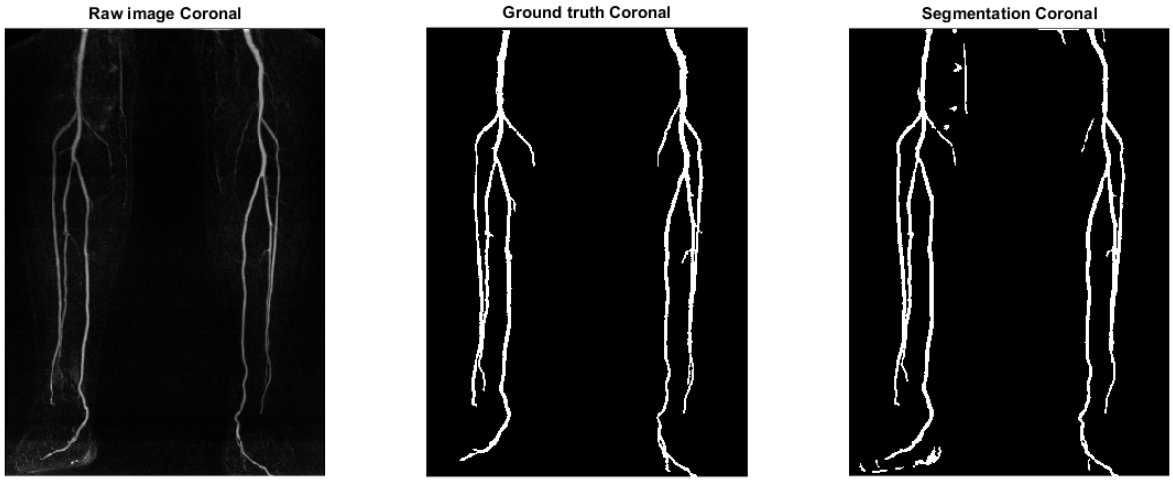

Figure 4.27: Segmentation with SVM

4.8 Results

Table 4 shows the final DSC results for Station 4:

Method	Level set	Frangi + thresh	OOF + Thresh	OOF + SVM
DSC	0.7737	0.7392	0.6859	0.8514

Table 4.4: Dice coefficient results for Station 4

4.9 Summary and conclusions

Method	Level set	Frangi + thresh	OOF + Thresh	OOF + SVM
Station 1	0.457	0.394	0.529	**0.587**
Station 2	**0.831**	0.674	0.777	0.806
Station 3	**0.721**	0.453	0.511	0.714
Station 4	0.774	0.739	0.686	**0.851**
Overall (mean)	0.696	0.565	0.626	**0.740**

Table 4.5: Dice coefficients results of all the stations

The aim of this project was to compare different vessel segmentation algorithms in order to determine which approach produced the most accurate results, as compared to manual segmentation, when applied to whole-body MRA scans of real patients. In this chapter we have seen four different methods: the level set method, the global threshold applied to Frangi and OOF filters and the classifier of single voxels with OOF features. Tab.4.5 summarizes the best results achieved at each station for all four algorithms, given as the Dice coefficient where a score of 1 indicates perfect agreement with the ground truth. We can see that the level set and the classification with SVM give in general the best results through all the stations. The Frangi and the OOF filters with a simple threshold are very quick in terms of computation but are less reliable for volumes with more complex structures, such as the vein artifacts in station 3. The level set is giving better results in station 2 and 3, but this is mainly due to additional non-arterial structures present, which could potentially be corrected with further post- processing. In Fig. 4.21 demonstrates that by removing the connected components, for example, we can improve upon the results of the level set.
Another important consideration is evident in the results of Station 1. We can see that the parameters that have been selected for the level set method in patient 70020 did not perform very well in the testing set. This is probably due to the fact that the level set is less robust to inter-patient variability than a classifier that uses vessel features, so, despite the normalization step, this method needs to be used carefully.
From our study, we can therefore conclude that the classifier approach gives the results for the task of artery segmentation. The main shortcoming of our implementation is that by only using features extracted from vesselness filters, the algorithm is unable to distinguish between arteries of interest and unwanted vessel-like structures (e.g. the pulmonary arteries and veins). This can be partially solved by post-processing as we said before but there is the need of finding a filter more aware of the shape, position and most of all context of the vessels. In the final chapter we will propose some potential future work to address this problem by introducing the concept of *context filters*.

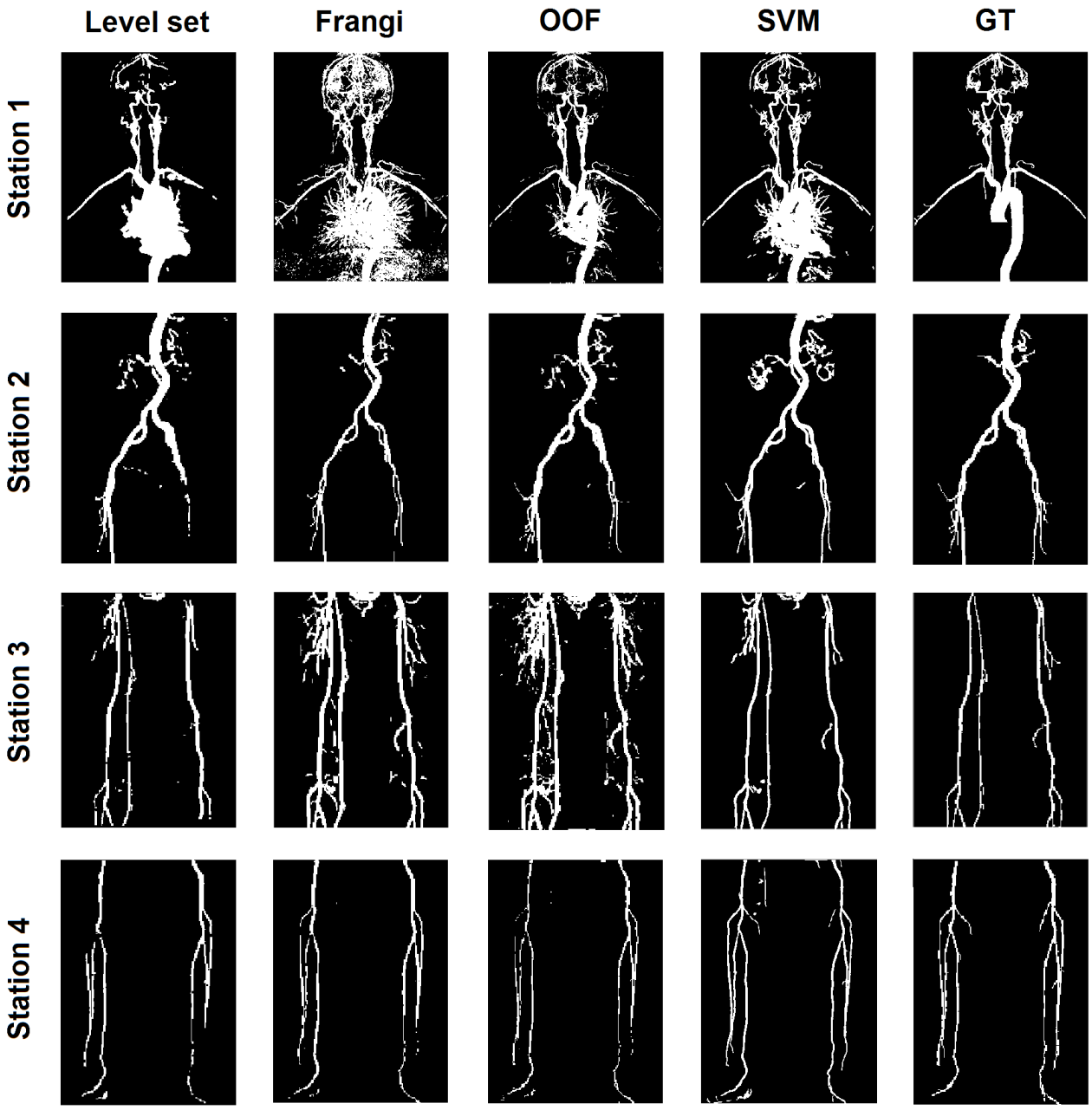

Figure 4.28: Segmentation on all the station with the each method

CHAPTER

5

FUTURE WORK

The main issues with training a segmentation classifier based purely on vesselness filters such as OOF are twofold;

- The low number of features
- Poor information on the context

The OOF fliter for example, gives information on the position of a likely vessel voxel in the form of its response to filters of varying radii (typically a max of around 15–20 for our datasets). This does not offer many discriminative features for the classifier to learn. There also the risk of giving redundant data to the classifier, so the efficiency of the segmentation can be affected.
Another negative attribute of this method as been introduce in the last Chapter. The information given by the vessel map at each scale is obtained by local computation voxel-by-voxel, so the algorithm can not be effective for categorize vein rather than arteries. The results on the leg station and the artifacts given by the complex pulmonary tree in the thorax are an evident example.
A potential direction for future work to improve upon these results would therefore be to develop filters capable of distuinguishing between different vessel-like structures. In this Chapter we propose a solution for this problem that can be done by filters that extract information based on the *context*.

5.1 High level filters

The idea of extracting information from the context in computer vision is based on different interpretations: taking images of part of an object can put together to classify the object itself (for example the tires and a pair of lights can define a car); two or more object can define another one (the car can suggest the presence of the road). In our case the context can extract information form different parts of the arteries which would help the categorization of the vessels.
In a probability point of view, the usage of context with the map given by filters like OOF is similar to creating a model that incorporates prior and likelihood information as in Bayes theory[14]. This *hybrid* method (HM) will give to the classifier two kind of features:

- the *image feature* computed locally, voxel-by-voxel
- the *context information* obtained with patches having different sizes

In literature, an example of usage of this concept is the one proposed by Annunziata et Trucco in [15] and [16] for vessel segmentation in retinal images. The work combines an appearance model, based on a special vessel detector called SCIRD that performs an enhancement of tubular structures like Frangi and OOF, with multi-range context filters. In this Chapter we will describe briefly this method then we will propose a possible application on our work.

5.1.1 Filter learning

In this section we do not explain the mathematical background of the SCIRD detector, but the aim and results of this filter are similar to the OOF, that is a creation of a *vessel map* similar to the one seen in the Chapter 2 and 4.
The first goal of [15] and [16] is to search a new representation of the given vessel map $\mathbf{x}$ by finding a linear combination of basis vectors ϕ_i:

$$\mathbf{x} = \sum_{i=1}^{k} a_i \phi_i \tag{5.1}$$

where ϕ needs to define an *over-complete* set of basis vectors to represents data efficiently. The reason why ϕ should be an over-complete basis is that they are better able to capture structures inherent in the input data, this is why they have to include the property of *sparsity*.
The sparsity can be obtained under the requirement of few coefficient $0 \ll a_i$ so all the other components will be near zero. The utility of this criterion can be motivated by the fact that all the images, especially the one containing different shapes of objects, can be seen as a superposition of elementary data as the one that can be obtained by this sparse matrix [17]. This atomic elements have more discriminative power so the classification can be more accurate. The Eq. 5.1 express the goal of learning a sparse dictionary of basis vector $D \in \Re^{q \times R}$ so the image can be projected in the code vector (ϕ) that minimize the reconstruction error.

There are different ways to approach the sparse representation problem, the one that have been used in the work of Annunziata et al. is the K-means unsupervised learning presented in [18]. The works try to learn sparse projection under two main constraints given by the utilization of the clustering:

- a sufficient testing set, compared to the dimension of the data
- application of normalization and whitening of the data

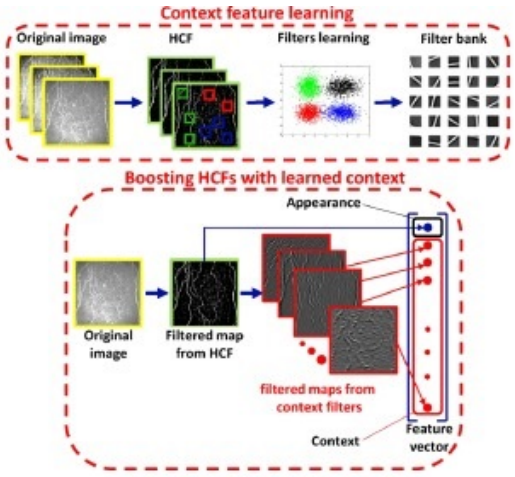

Figure 5.1: In the figure we can see the idea of context learining of [15] and [16]

So before performing the learning by K-means there is the need to normalize each patch $\mathbf{x}^{(i)}$ of the chosen dimension, then apply a ZCA whitening as:

$$\mathbf{x}_{ZCA}^{(i)} = V(\Sigma + \epsilon_{ZCA} I)^{-1/2} V^T \mathbf{x}^{(i)} \tag{5.2}$$

where V and Σ are the matrix that contains respectively the eigenvectors and the eigenvalues of the covariance matrix of the patch $\mathbf{x}^{(i)}$.
After this quick pre-processing step they solved the optimization problem of Eq. 5.1, rewrite as:

$$argmin \sum_i \left\| D\mathbf{c}^{(i)} - \mathbf{x}^{(i)} \right\|_2^2 \tag{5.3}$$

where D contains the coefficients a_i and $\mathbf{c}$ represents the basis vectors.
The final step to obtain the minimization and the sparsity is to perform the K-mean until convergence of the loop:

$$\forall c_j^{(i)} \in C \doteq \begin{cases} D^{(j)T} x^{(i)} & if\ j = \max_l |D^{(l)T} x^{(i)}| \\ 0 & otherwise \end{cases}$$

$$D \doteq XC^T + D$$

$$D^{(j)} \doteq D^{(j)} / \left\| D^{(j)} \right\|$$

At the end of the algorithm a dictionary is learned, so is then possible to combine the feature extracted by SCIRD detector.
The study then propose the extraction of the context information by the correlation of the learned filters with the raw data and with a downscale version of the same image. This downscaling step can be done n times but it gives already good results with $n = 3$. These *context feature* are then used in a random forest classifier with the results of the enhancement done by SCIRD.
The works at the end shows that the result overscore completely the state-of-art of hand crafted features methods.

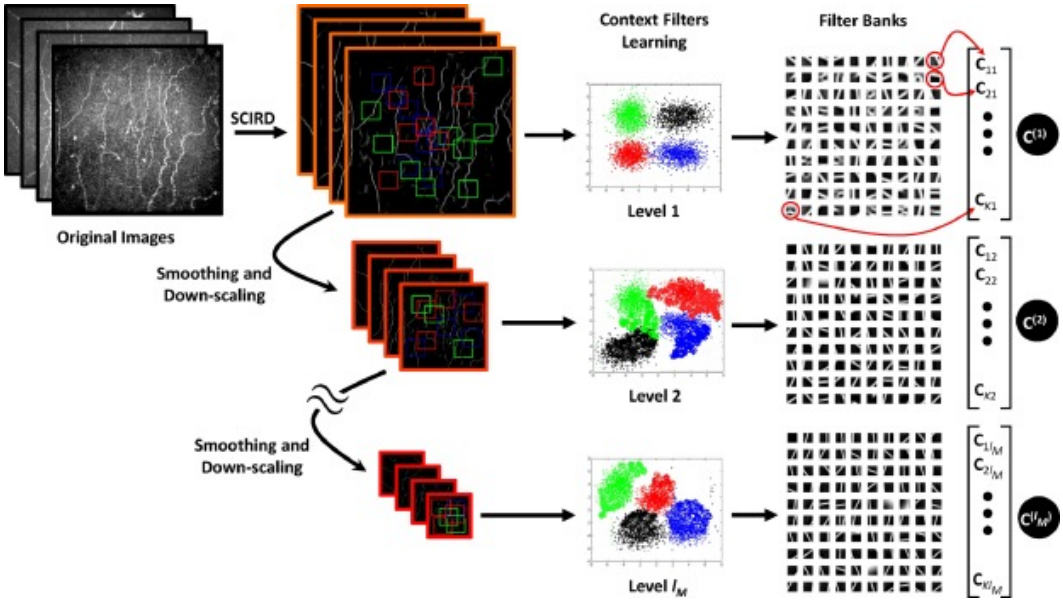

Figure 5.2: The downscaling that hase been used for the feature extraction

5.2 Conclusions

The dataset of this project has a different dimensionality than the one from Annunziata et al., we had in fact to process 3D data instead of 2D images like the one from the retina. Therefore, each step discussed previously must be extended to a higher dimensional space.
If the K-mean algorithm can be done in a similar way, what is more critical is the whitening in three dimension. For this reason the data have to be treated as a tensor and the decomposition in order to find the matrix V and Σ has to be multilinear.
A possible filter bank that can be learned is showed in Fig.

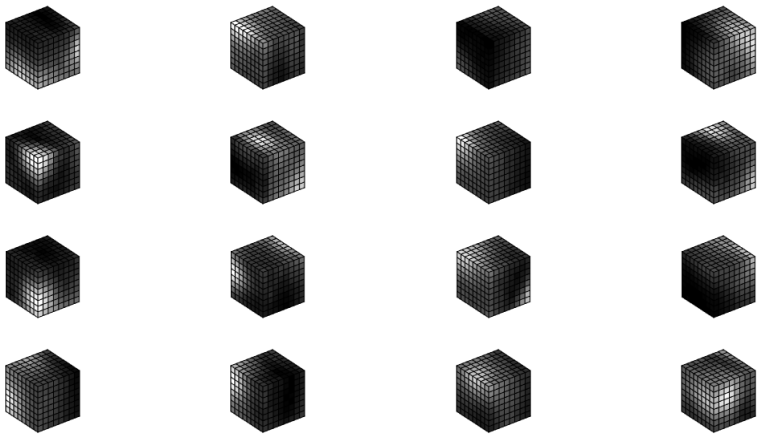

Figure 5.3: An example of filters learned by k-means on the MRA dataset

Another suggestion for possible future work is a new classifier than the one that has been used in this thesis (SVM with RBF kernel). The number of features is too huge for being computed by this kind of SVM so the training and testing can be really time consuming. A good solution can be the random forest as proposed in Annunziata.

IMAGE LINKS

https://math.berkeley.edu/~sethian/2006/Semiconductors/ieee_level_set_explain.html
https://upload.wikimedia.org/wikipedia/commons/2/2a/Svm_max_sep_hyperplane_with_margin.png
http://sebastianraschka.com/images/faq/evaluate-a-model/k-fold.png

REFERENCES

[1] Nichols M., Townsend N., Scarborough P., Rayner M., *Cardiovascular disease in Europe 2014: epidemiological update*, European Heart Journal Aug 2014, 2014.

[2] Lesage D., Angelini Elsa D., Bloch I., Funka-Lea G., *A review of 3D vessel lumen segmentation techniques: Models, features and extraction schemes*, Medical Image Analysis, 2009 , Volume 13 , Issue 6 , 819–84.

[3] Gonzales R., Woods R., *Digital Image Processing*,Prentice Hall,2007

[4] Chan T.F., Vese L.A., *Active contours without edges*, IEEE Transactions on Image Processing 2001, 10(2): pp. 266–277.

[5] Zhang Y., Matuszewski B. J., Shark L. K., Moore C. J., *Medical Image Segmentation Using New Hybrid Level-Set Method*, BioMedical Visualization, 2008. MEDIVIS '08. Fifth International Conference, IEEE, 9-11 July 2008.

[6] Kass M., Witkin A., Terzopoulos D. *Snakes: Active contour models*, International Journal of Computer Vision,1988, 1:321-331.

[7] Sethian J.A. *Level Set Methods and Fast Marching Methods : Evolving Interfaces in Computational Geometry, Fluid Mechanics, Computer Vision, and Materials Science.* Cambridge University Press,1999.

[8] Brieva J., Gonzalez E., Gonzalez F., Bousse A., Bellanger J. J., *A Level Set Method for Vessel Segmentation in Coronary Angiography*, 2005 IEEE Engineering in Medicine and Biology 27th Annual Conference, 2005.

[9] Szymczak A., Tannenbaum A., Mischaikow K.,*Coronary vessel cores fromÂ£D imagery: a topological approach.*, Proc. SPIE Med. Imaging, 2005 , Volume 5747 , 505 – 513.

[10] Frangi A.F., Niessen W.J., Vincken K.L., Viergever M.A., *Multiscale vessel enhancement filtering.* In: Proc. Med. Image Comput. Assist. Interv., 1998, vol. 1496, pp. 130–137.

[11] Law M.W.K., Chung A.C.S., *Three Dimensional Curvilinear Structure Detection using Optimally Oriented Flux*, ECCV 2008, pp. 368–382.

[12] Otsu N., *A threshold selection method from gray-level histograms*, IEEE Trans. Sys., Man., Cyber., 1979, vol. 9, pp. 62–66.

[13] Boser B. E., Guyon I., Vapnik V., *A training algorithm for optimal margin classifiers.*, Proceedings of the Fifth Annual Workshop on Computational Learning Theory, 1992, ACM Press, pages 144–152.

[14] Tu Z., Bai X., *Auto-context and its application to high-level vision tasks and 3d brain image segmentation*, IEEE TPAMI, 2010.

[15] Annunziata R., Kheirkhah A., Aggarwal S., Hamrah P., Trucco E. *A Fully Automated Tortuosity Quantification System with Application to Corneal Nerve Fibres in Confocal Microscopy Images*, Medical Image Analysis, 2016.

[16] Annunziata R., Trucco E. *Accelerating Convolutional Sparse Coding for Curvilinear Structures Segmentation by Refining SCIRD-TS Filter Banks*, IEEE TMI, 2016.

[16] Annunziata R., Trucco E. *Accelerating Convolutional Sparse Coding for Curvilinear Structures Segmentation by Refining SCIRD-TS Filter Banks*, IEEE TMI, 2016.

[17] *Sparse Coding* Deep Learning lessons, Computer Science Department, Stanford University

[18] Coates A., Ng A.Y., Learning feature representations with k-means, in: Neural Networks: Tricks of the Trade, 2012, Springer, pp. 561–580.